Sustainable Energy & Fuels

Interdisciplinary research for the development of sustainable energy technologies

Accepted Manuscript

This article can be cited before page numbers have been issued, to do this please use: H. Idriss, *Sustainable Energy Fuels*, 2026, DOI: 10.1039/D6SE00124F.

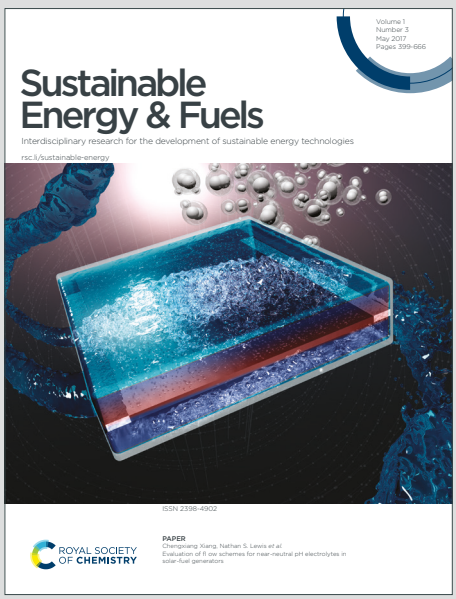

This is an Accepted Manuscript, which has been through the Royal Society of Chemistry peer review process and has been accepted for publication.

Accepted Manuscripts are published online shortly after acceptance, before technical editing, formatting and proof reading. Using this free service, authors can make their results available to the community, in citable form, before we publish the edited article. We will replace this Accepted Manuscript with the edited and formatted Advance Article as soon as it is available.

You can find more information about Accepted Manuscripts in the Information for Authors.

Please note that technical editing may introduce minor changes to the text and/or graphics, which may alter content. The journal's standard Terms & Conditions and the Ethical guidelines still apply. In no event shall the Royal Society of Chemistry be held responsible for any errors or omissions in this Accepted Manuscript or any consequences arising from the use of any information it contains.

ROYAL SOCIETY OF CHEMISTRY

rsc.li/sustainable-energy

View Article Online
DOI: 10.1039/D6SE00124F

Study of reduced states of $Ce_{1-y}Fe_yO_2$ and $Ce_{1-y}U_yO_2$ for the thermochemical water splitting to hydrogen.

Hicham Idriss

Department of Chemistry, University College London, London WC1E 6BT, U.K

Abstract

Solar thermochemical water splitting (TCWS) is a promising approach for sustainable hydrogen production using concentrated solar energy. Cerium oxide (CeO_2) is one of the most studied redox materials for this process due to its fast oxidation kinetics and structural stability at high temperature. However, its practical implementation remains limited by the high reduction energy required to reach significant non-stoichiometry, which restricts hydrogen yields. In this review, key fundamental aspects of ceria reduction and defect formation are discussed, with a focus on strategies to enhance reducibility through partial substitution of Ce cations by transition metals and actinides. In particular, substitution with Fe or U promotes the formation of oxygen vacancies (for different reasons, as discussed) and stabilizes reduced states, thereby increasing the extent of reduction and improving hydrogen production. Experimental and theoretical studies on $Ce_{1-y}Fe_yO_{2-\delta}$ and $Ce_{1-y}U_yO_{2\pm\delta}$ are reviewed, including insights from temperature-programmed reduction, core- and valence-level X-ray photoelectron spectroscopy, and DFT+U calculations. Test reactions show, in line with spectroscopic results, that small fractions of Fe^{3+} or U^{4+} gave highest Ce^{3+} and TCWS reaction yields, while increasing the dopant fraction decreases the reaction yield. The correlations between reduction behavior, oxygen vacancy formation, charge-transfer phenomena, and hydrogen yields are discussed, with emphasis on the need for fundamental understanding of reduction energetics as a key factor for advancing solar thermochemical hydrogen generation.

Keywords

Mixed oxide $Ce_{1-y}M_yO_2$; thermochemical water splitting (TCWS) reaction to hydrogen; XPS U4f, XPS Ce3d; Ce^{4+} reduction to Ce^{3+}; U^{4+} oxidation to U^{5+} and U^{6+}; DFT + U computation of oxygen vacancies formation energy; XRD of UO_2, U_3O_8, and CeO_2; TEM of $Ce_{1-y}Fe_yO_2$ and $Ce_{1-y}U_yO_2$; TPR of $Ce_{1-y}Fe_yO_2$ and $Ce_{1-y}U_yO_2$; (111) epitaxy of $Ce_{1-y}U_yO_2$.

View Article Online
DOI: 10.1039/D6SE00124F

Table of contents

1. Introduction

The Thermo-Chemical Water Splitting (TCWS) reaction is a solar driven H_2 production from water using a redox type process of suitable materials. This short review's focus is on reducible oxides as the material of choice. The reaction has received considerable attention these last few decades [1,2,3] and the process is a two-step reaction. The first one is endothermic, in which an oxide material in binary or mixed phases is reduced at a high temperature in inert environment releasing a fraction of its oxygen atoms as O_2. Temperatures as high as 1500 ^oC are typically needed to ensure a reduction suitable for

View Article Online
DOI: 10.1039/D6SE00124F

studies and with a potential for application (equation 1). The second step is exothermic, where the reduced oxide(s) is exposed to H_2O vapor, typically conducted a few hundred degrees lower in temperature. In this second step the reduced oxide is oxidized back and H_2 is released (equation 2). Therefore, H_2 and O_2 are produced separately. The following two equations present these two steps.

$$MO_x \rightarrow MO_{x-\delta} + \delta/2\ O_2 \qquad \textit{Equation 1}$$

$$MO_{x-\delta} + \delta\ H_2O \rightarrow MO_x + \delta\ H_2 \qquad \textit{Equation 2}$$

Where M is a metal cation, x is for the compound stoichiometry (2 in the case of CeO_2 for example) and δ is the extent of reduction, $\delta < x$ (typically a small fraction of x).

This reaction performs similarly for CO_2 to CO reduction. When the energy input is provided from the sun, it uses a large fraction of the solar spectrum making it among of the most efficient [4,5] known systems for H_2 generation from water with theoretical efficiencies > 40%. It is still in the research phase largely because of the cost associated to the solar concentrators needed for the reduction.

The dynamics of the reduction and oxidation of metal oxides affect their properties and these in turn, dictates their performance in many applications, and that includes other processes beside the TCWS or CO_2 reduction such as in redox-driven reactions in catalysis [6] and gas sensors []7. Cerium oxide (CeO_2/CeO_{2-x}, $x < 0.5$) stands out as one of the most active and stable reducible metal oxides [8] and is therefore prone to many fundamental studies largely because of its relatively simple structure (fluorite), simple surface termination dominated by the (111) face, and localized charges upon the creation of oxygen defects; when compared to many other solar materials.

It is worth making a distinction between the TCWS cycle and a hydrocarbon-based catalytic cycle as it is in practice at present. In catalysis, the reduction of an oxide, is conducted by using a chemical compound (providing the chemical energy), such as H_2 [9] or CO [10]. H_2 and CO are largely generated by steam methane reforming and therefore contribute to CO_2 emission, that is why solar thermal-driven alternatives are desired when looking beyond a hydrocarbon-based energy system. The main challenge for this alternative process is the large input of energy needed for the reduction step. To this end, considerable amount of work addressing the reduction of CeO_2 in order to understand its steps at the fundamental and applied levels is pursued. Many computational studies have indicated that the energy needed to create an oxygen vacancy in the bulk of CeO_2 is about 3 eV [11,12,13], while the energy required for atomic oxygen diffusion [14] is less ≈1 eV. Despite the relatively fast reaction kinetics for the redox cycle, which is highly desired for the two steps described by equations 1 and 2, the high energy cost makes the process unsustainable. At present, estimates of the levelized cost of H_2 [LCOH: the cost

View Article Online
DOI: 10.1039/D6SE00124F

of making H_2 before making profit after a number of years, typically 20 years] produced by the TCWS method is close to 10 USD per kg, which is about five times higher than the present cost from fossil fuels) [15]. Because the TCWS reaction solely relies on the O-defect density, which is, per mass, low in CeO_2 many approaches have been pursued to mix CeO_2 with other metal cations to decrease the reduction energy and consequently increase the density of the reduced state [16].

Among the few methods used the following two are of focus of this review.

A. Charge transfer: a fraction of Ce^{4+} cations is substituted with metal cations that can donate electrons and themselves be oxidized. For example, the substitution of Ce^{4+} with U^{4+} was found to enhance the reduction of CeO_2, particularly at low levels, refs. 12, 13. Upon the removal of an oxygen atom (two electrons are left in the lattice), in a pure CeO_2 two Ce^{4+} cations are reduced by these two electrons to Ce^{3+} cations. However, in the presence of U^{4+} three Ce^{3+} cations are formed (instead of two), and one U^{4+} cation is oxidized to a U^{5+} cation, as per the following equation.

$$Ce^{4+}(4f^0) + U^{4+}(5f^2) \rightarrow Ce^{3+}(4f^1) + U^{5+}(5f^1) \qquad \textit{Equation 3}$$

For a charge-transfer mechanism to occur between two cations in a mixed oxide, several conditions should ideally be satisfied:

(i) the substituting cation should have an ionic radius close to that of the host cation,

(ii) it should possess the same (initial) oxidation state, and

(iii) the corresponding oxide should have a similar crystal structure to the host material, which increases the likelihood of forming homogeneous solid solutions. [17].

Yet, the optimal fractional substitution for the reduction of Ce cations is not straight forward to know because statistical entropy (distribution of U^{4+} cations around Ce^{4+} cations) affect the electron transfer process, and in addition phase segregation may still occur depending on the environment (oxidizing vs reducing). The redox properties of such a system have been experimentally studied in the past [18,19,20,21]. Experimental evidence of charge transfer was found, and the optimal charge transfer between Ce and U cations occurred at. low % of U. In these studies, the mixed oxide $Ce_{1-y}U_yO_{2\pm\delta}$ was reduced by H_2 at 973 K to prevent phase segregation or by Ar^+ sputtering for the core level spectroscopy measurements to monitor the charge transfer. For hydrogen production from water, experimental results showed, in line with spectroscopy, that low levels of U substitutions were better than higher levels, with an experimental optimal of about 10%. Moreover, spectroscopic studies of the Ce and U oxidation states of an epitaxy of the mixed oxide with (111) surface termination have largely confirmed the polycrystalline results [22].

View Article Online
DOI: 10.1039/D6SE00124F

B. Charge compensation (alio-valency): this is generally viewed as due to lattice distortion because of the difference in the cations' size and charge. The substitution of Ce^{4+} with these metal cations, of a lower oxidation state, creates vacancies. These vacancies are not associated to excess electrons and therefore there is no increase/decrease in electron charge. A large number of elements were studied for this, and most showed that indeed Ce^{4+} reduction to Ce^{3+} was enhanced. The addition of cobalt (Co) enhanced CeO_2 reduction during the photoreduction [23] of CO_2 to CH_4 and COS hydrolysis [24] reactions. Praseodymium (Pr), where Pr^{3+} increases the creation of oxygen vacancies and Pr^{4+} increases the oxygen storage capacity [25]. Manganese (Mn), enhanced oxygen mobility via vacancy formation [26]. Computationally, a large body of work has also been conducted to study the creation of oxygen vacancies upon alio-valent cation substitution, **table 1**. Among them: Mn (DFT + U and HSE06) [27] , Cu (DFT + U) [28] , Ni (DFT + U and HSE06) [29] and (DFT + U) [30], and Fe (DFT +U). These results indicated that the oxygen vacancy formation energy is lower when compared to ceria alone [31,32].

Table 1.

Representative DFT computed values for oxygen vacancy formation energy of $Ce_{1-y}M_yO_2$ (E) and vacancy migration barrier. M is the element added to CeO_2, and y is the element fraction. [Near and far are with respect to the metal cation used.]

Element	**E (eV)**	**Migration barrier (eV)**	**References**
Fe^{3+}	1 - 1.5	-	[33]
Zr^{4+}	≈ 2 ($Ce_{0.875}Zr_{0.125}O_2$)	< 1	[34] [35]
La^{3+}	1.3 (near) 1.6 (far)	0.7	[36,37]
Nb^{5+}	2.3 (near) 2.9 (far)	0.6-0.8	[35, 38]
U^{+4}	2.7	-	[12-13]

Among the aliovalent systems, solid solutions of CeO_2 containing Fe^{3+} have been studied in some details. In one of these works it was found that substituting a fraction of Ce^{4+} by Fe^{3+} cations in CeO_2 led to a decrease of the activation energy for the selective catalytic reduction reaction of NO by half [39]. This was attributed to the formation of a distorted Fe–O–Ce structure. DFT calculation and titration via pyridine-adsorption indicated that this Fe–O–Ce structure has increased the number of Lewis acid sites

View Article Online
DOI: 10.1039/D6SE00124F

as well as the charge density around Ce cations when compared to those of pure CeO_2. The authors also found that low Fe fraction ($x < 0.3$) kept the fluorite structure (solid solution) via a vacancy compensation mechanism, leading to an increase in oxygen vacancies which was linked to increase of the catalytic performance. Other work has shown the presence of a considerable fraction of Ce^{3+} cations by analyzing the XPS Ce3d lines (at ca. 885 eV and 904 eV (V' and U' lines)) upon the introduction of Fe^{3+} cations into the lattice of $Ce_{0.8}Fe_{0.2}O_{2-\delta}$ [40,41] (δ: deviation from stoichiometry). Also, other have shown that Fe substitution of less than 30% increased the number of oxygen vacancies [42] and improved CO conversion to CO_2 the latter is attributed to the formation of more mobile oxygen atoms in the redox cycle [43] . In another study, Fe 5 at.% was tested at 1823 K and found to be more active (a higher production rate per unit weight) and faster (a higher rate of release of hydrogen) than CeO_2 alone for the same reaction. Phase segregation, however, occurred due to the very high thermal reduction, 1823 K, temperature [44].

The performance of pristine and cation substituted CeO_2 in TCWS has been systematically studied, revealing that these metal cation can lower reduction temperatures, increase δ, and improve H_2 yield per cycle. However, trade-offs with stability and phase segregation remain critical.

Table 2.

Examples of reported performance of CeO_2 and mixed oxide-CeO_2 based systems for the thermochemical water splitting reaction. a: reduced by Ar ions sputtering.

Material	**Conditions (T, atm)**	**δ or O_2 released**	**H_2 yield per cycle**	**References**
CeO_2 (bulk)	1773 K	$\delta < 0.02$	~10 mL H_2 g^{-1}	[45,46,47,48]
$Ce_{0.9}Zr_{0.1}O_2$	1673 K	δ ~ 30% vs CeO_2	~10 mL H_2 g^{-1}	[49]
$Ce_{0.9}Fe_{0.1}O_{2-\delta}$	1673-1823 K	up to 50 μmol O_2 g^{-1}	~20–25 mL H_2 g^{-1}	[50]
$Ce_{0.9}U_{0.1}O_{2\pm\delta}$	973–1200 K [a]	Ce^{3+} fraction [a] > 50%	~18–22 mL H_2 g^{-1}	[20]
$Ce_{0.8}Pr_{0.2}O_{2-\delta}$	1773 K	~15 mL O_2 g^{-1}	~ 4 mL H_2 g^{-1}	[51,52]
$Ce_{0.8}Mn_{0.2}O_{2-\delta}$	1773 K	Fast vacancy migration	~ 4 mL H_2 g^{-1}	[53,54]

The review focuses on two systems for which complementary information has been obtained using a combination of techniques, including spectroscopy, diffraction, microscopy, and thermochemical performance measurements. This two systems are composed of Fe and U cations used (separately) as substituents to enhance the reduction of CeO_2. A particular attention is given on phase segregation studied by XRD, charge transfer studied by core- and valence-level spectroscopy, and reduction temperature by TPR, all on polycrystalline samples. Also, core level spectroscopy results of single

View Article Online
DOI: 10.1039/D6SE00124F

crystals of the mixed $Ce_{1-y}U_yO_2$ grown by epitaxy complemented by DFT+U computations are presented.

2. X-ray diffraction ($Ce_{1-y}Fe_yO_2$ and $Ce_{1-y}U_yO_2$)

Figure 1 presents XRD patterns of CeO_2, and $Ce_{0.95}Fe_{0.05}O_2$ that were heated at the indicated temperatures.

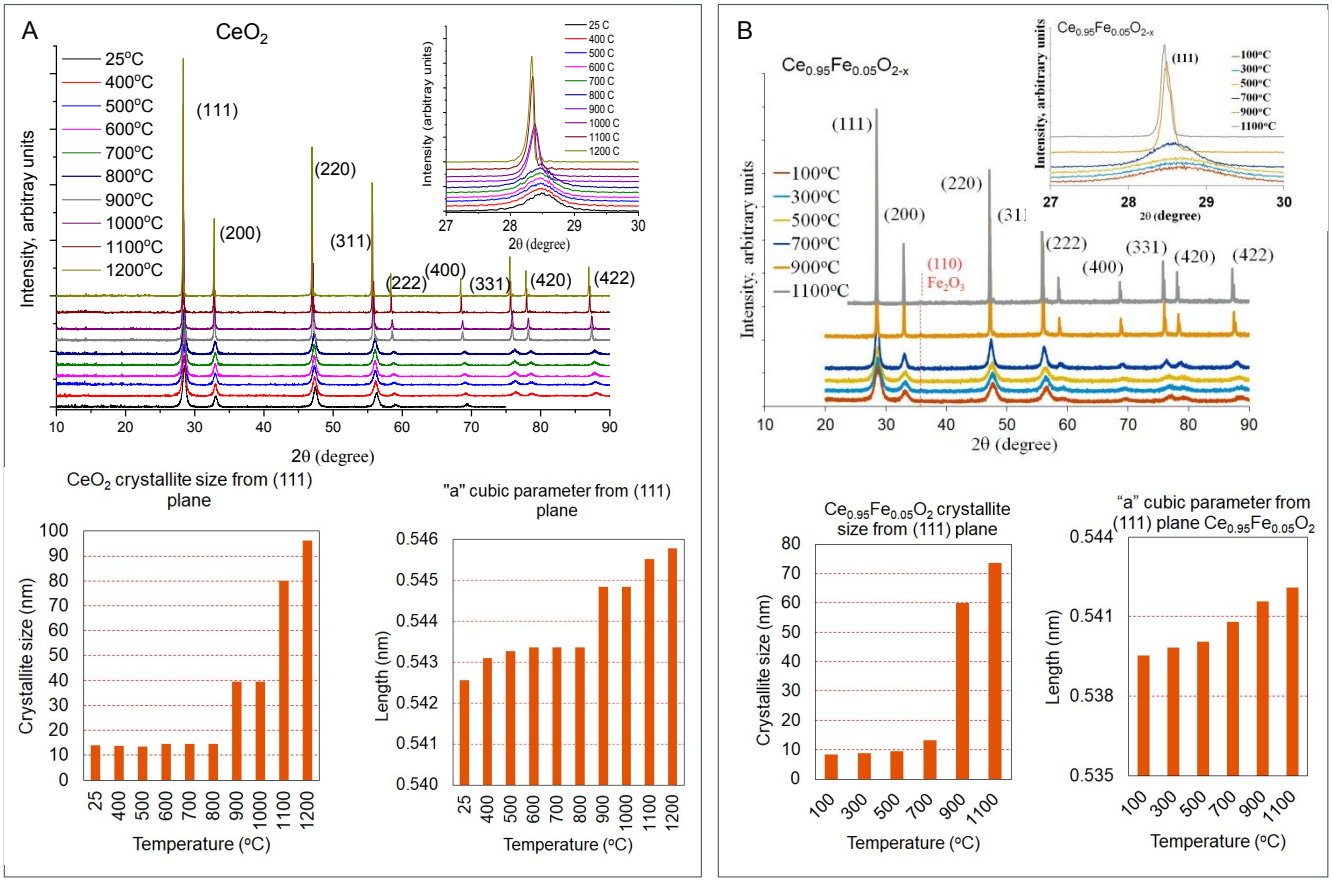

Figure 1.

(A) XRD patterns of CeO_2 together with the extracted crystallite size and cubic parameter from the (111) lines; inset: a zoom on the (111) diffraction line to highlight the shift in angle and narrowing of the Full Width Half Maximum (FWHM) with increasing temperature in ambient environment. (B) Contains similar results for $Ce_{0.95}Fe_{0.05}O_2$. From Ref. [50], permission License number 6133081449846

The diffraction pattern of CeO_2 shows a nano size dimension (L ≈ about 14 nm) for the "as prepared" oxide, with a lattice parameter (**a**) = 0.543 nm (**figure 1A**). Crystalline CeO_2 gives rise to strong lines at 2θ = 28.5º, 33.0º, 47.5º, 56.4º for the (111), (200), (220) and (311) respectively, whose positions and

View Article Online
DOI: 10.1039/D6SE00124F

Full Width Half Maximum (FWHM) being sensitive to its crystallite dimension and degree of crystallinity. No change in these parameters is seen up to ca. 900 ^{o}C (1173 K). At this temperature L considerably increased to 39 nm (due to sintering) together with an increase of **a (**0.545 nm) (due to bulk reduction). At 1100 ^{o}C, L doubled to 80.2 nm and a further increase of **a** (0.546 nm) is seen. Hematite Fe_2O_3 gives lines at 2θ= 33.3^{o}, 35.7^{o} and 62.3^{o} for the (104), (110) and (214) lines, respectively. Because Fe^{3+} (0.6Å) ions are much smaller than Ce^{4+} ions (ca. 1 Å in octahedral coordination) their incorporation into the lattice can be monitored mostly by a positive shift of 2θ which is associated with a broadening of the lines due to the formation of smaller crystallites [55]. Therefore, both the shift and the absence of Fe_2O_3 lines are often taken as a strong indication of the presence of a solid solution. Depending on the preparation method this is found to be up to about 0.3-0.4 atomic ratio Fe^{3+}/Ce^{4+} cations [56]. The addition of Fe to CeO_2 appears to be substitutional since no other diffraction lines attributed to Fe_2O_3 were seen up to 900^{o}C or so. Segregation occurred at 1100^{o}C where diffraction lines corresponding to Fe_2O_3 (110) and (003) are observed. **Table 3** compares the parameters of three oxides at 500^{o}C and 1100^{o}C.

Table 3.

Crystallite size and cubic lattice dimension for CeO_2 and $Ce_{1-y}Fe_yO_2$ at 773 K and 1373 K. Data extracted from **figure 1**. From Ref. [50], permission License number 6133081449846

oxide	2θ CeO_2 (111) at 773 K	Crystallite size at 773 K (nm)	Cubic lattice parameter at 773 K (nm)	Crystallite size at 1373 K (nm)	Cubic lattice parameter at 1373 K (nm)
CeO_2	28.46^{o}	14	0.543	80.2	0.545
$Ce_{0.95}Fe_{0.05}O_2$	28.68^{o}	9.5	0.540	73.6	0.542
$Ce_{0.75}Fe_{0.25}O_2$	28.84^{o}	6.5	0.540	61.3	0.544

Figure 2 presents XRD of as prepared $Ce_{0.5}U_{0.5}O_2$ and after it has been heated, in situ under N_2 atmosphere, at the indicated temperatures. XRD patterns related to the fluorite structure are identified with prominent (111), (200), (220) and (311) peaks at 2θ = 28.54^{o}, 33.11^{o}, 47.58^{o}, and 56.39^{o}, respectively. The crystallite dimension calculated from the (111) diffraction line is found close to 12 nm for the fresh oxide. Upon heating to 300^{o} C (573 K) other diffraction patterns at 2θ = 21.38^{o}, 26.16^{o}, 33.95^{o}, 43.58^{o}, and 51.68^{o} are seen. The patterns are attributed to other uranium oxide phases: orthorhombic α U_3O_8 or hexagonal α U_2O_5, or orthorhombic U_2O_5 [57,58]. Previous work has indicated

View Article Online
DOI: 10.1039/D6SE00124F

that in the process of oxidation of UO_2 to UO_3, U_3O_8 is formed [59] as the most stable phase; however, metastable U_2O_5 is also formed that eventually transform to α U_3O_8. The small crystallite structures and the broadening of the lines did not allow for further analysis. It is clear however, that some U cations in the solid solution segregate forming a more stable higher oxide that is attributed to either α U_3O_8 (or U_2O_5). Because the process occurs under N_2 environment, it is expected that CeO_2 left in the fluorite structure is reduced to $CeO_{2-\delta}$; this point will be reviewed in more details below.

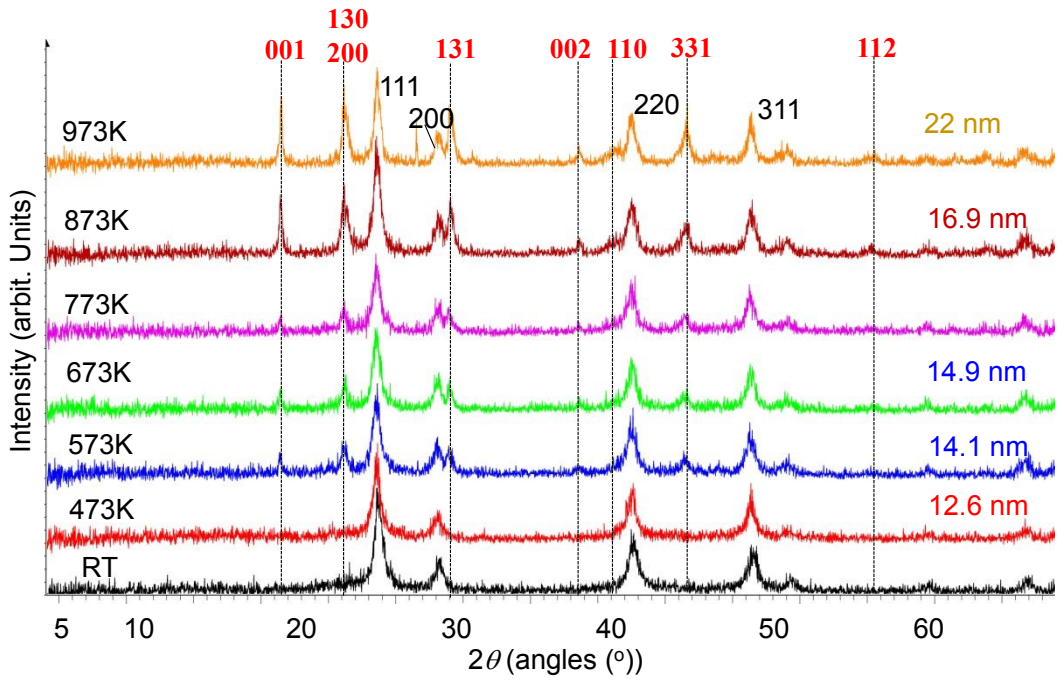

Figure 2.

In situ XRD of $Ce_{0.5}U_{0.5}O_2$ that was heated at the indicated temperatures. The numbers at the righthand side of the figure are those of crystallites size based on the (111) diffraction line of the fluorite structure at 2θ = 28.54° (d = 3.12 Å). The numbers (in red) on top of the dashed vertical lines in the figure are the diffraction pattern of α U_3O_8. From ref. 20, permission License number 6133100874303.

3. Transmission Electron Microscopy (TEM); $Ce_{1-y}Fe_yO_2$ and $Ce_{1-y}U_yO_2$.

Figure 3 presents the TEM, Selected Area Electron Diffraction pattern (SAED) and Energy Dispersive X-ray patterns (EDX) of $Ce_{0.95}Fe_{0.05}O_{2-\delta}$, and $Ce_{0.75}Fe_{0.25}O_{2-\delta}$ that were calcined at 773 K. Like the data of XRD, both presented the fluorite structure of CeO_2; no Fe_2O_3 phase is seen. The d spacing shows a

View Article Online
DOI: 10.1039/D6SE00124F

slight decrease in the case of $Ce_{0.75}Fe_{0.25}O_{2-\delta}$ when compared to $Ce_{0.95}Fe_{0.05}O_{2-\delta}$. Therefore, both microscopic and macroscopic diffraction methods indicate that the crystallite size of CeO_2 decreases with Fe substitution. From TEM the average crystallite size of $Ce_{0.95}Fe_{0.05}O_{2-\delta}$ is 8-10 nm while that of $Ce_{0.75}Fe_{0.25}O_{2-\delta}$ is 5-7 nm. The decrease of the crystallite size might be due to a decrease of the surface energy (more stable) when compared to that of CeO_2. EDX shows the presence of Fe in both mixed oxides with an intensity qualitatively tracking the expected concentration.

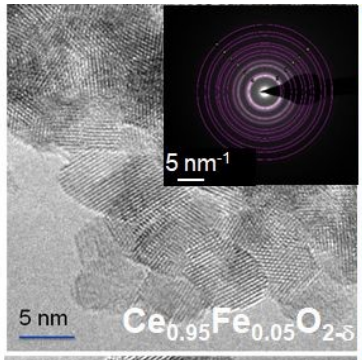

Ring	Radius (nm^{-1})	d (nm)	Lattice plane
1	3.125	3.21	111
2	3.623	2.77	200
3	5.117	1.98	220
4	6.002	1.67	311
5	7.213	1.39	400
6	7.917	1.27	331
7	8.841	1.13	422

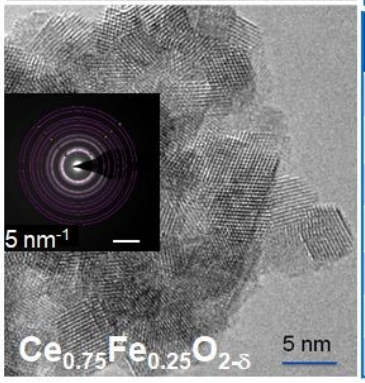

Ring	Radius (nm^{-1})	d (nm)	Lattice plane
1	3.125	3.20	111
2	3.623	2.76	200
3	5.117	1.95	220
4	6.002	1.67	311
5	7.213	1.39	400
6	7.917	1.26	331
7	8.841	1.13	422

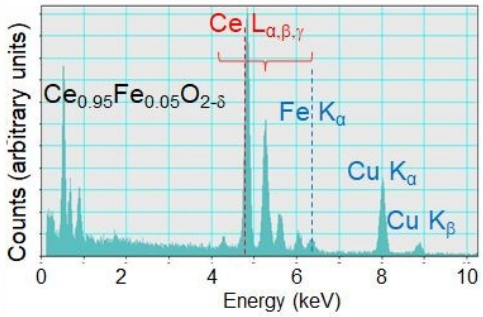

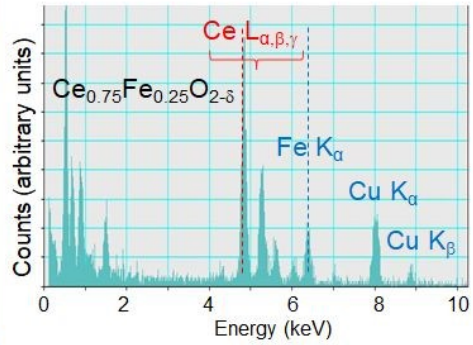

Figure 3.

Transmission Electron Microscopy (TEM), Selected Area Electron diffraction pattern (SAED) and Energy Dispersive X-ray patterns (EDX) of $Ce_{0.95}Fe_{0.05}O_{2-\delta}$, and $Ce_{0.75}Fe_{0.25}O_{2-\delta}$ that were calcined at 773 K. The values in the tables in the middle are extracted from the SAED in the inset of the TEM images and ring numbers starts with the center of the concentric circles (the bright spot of each inset). From Ref. [50], permission License number 6133081449846

A series of polycrystalline $Ce_{1-x}U_xO_{2\pm\delta}$ was synthesized and studied for their thermochemical water splitting to hydrogen. XRD, as shown above for the as-prepared mixed oxides, present a fluorite structure, in line with numerous other studies in which Ce and U cations have high miscibility [60,61,62] for the as prepared oxide. **Figure 4 A** (HR-TEM) indicates that particles are crystalline with a size of about 10 nm. Like in the case of Fe, data indicate a high miscibility of U cations in CeO_2. For example, while **Figure 4 B** (STEM) shows no distinction between the atoms while the EELS spectra of the same

View Article Online
DOI: 10.1039/D6SE00124F

area, **Figure 4 C**, shows the presence of both U and Ce; the Ce 3d→4f and U 4d→5f transitions. The lattice fringes obtained from the diffraction pattern (**Figure 4 D**) related to **Figure 4 B** are nearly identical to those of CeO_2.

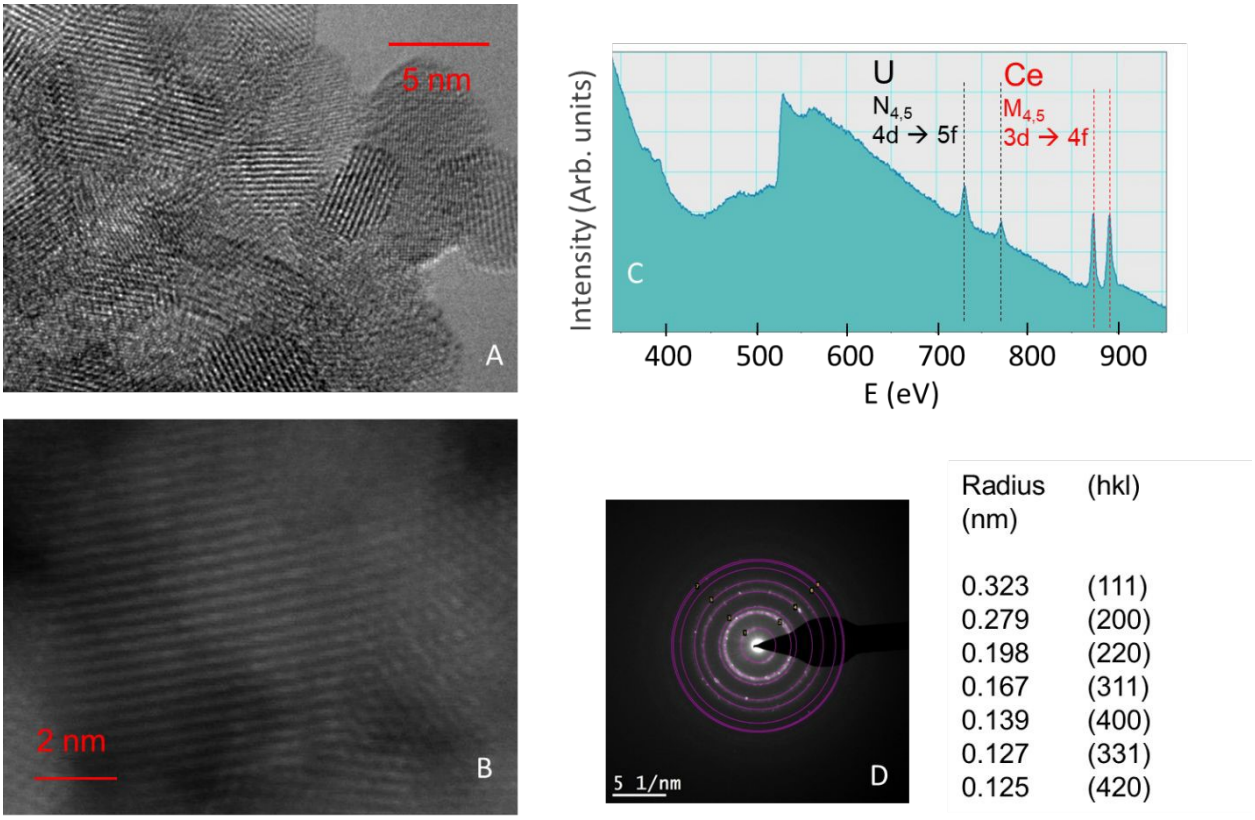

Figure 4.

A. High-resolution transmission electron microscopy (HRTEM) of $Ce_{0.75}U_{0.25}O_2$ polycrystalline mixed oxide. **B.** Scanning transmission electron microscopy (STEM) of a selected area from A. **C.** Electron energy loss spectroscopy (EELS) spectrum of the area shown in B. **D.** Selected area electron diffraction (SAED) of B. From ref. 22 (no permission is needed: Creative Commons Attribution 4.0 License).

View Article Online
DOI: 10.1039/D6SE00124F

4. Temperature Programmed Reduction (TPR) ($Ce_{1-y}Fe_yO_2$ and $Ce_{1-y}U_yO_2$).

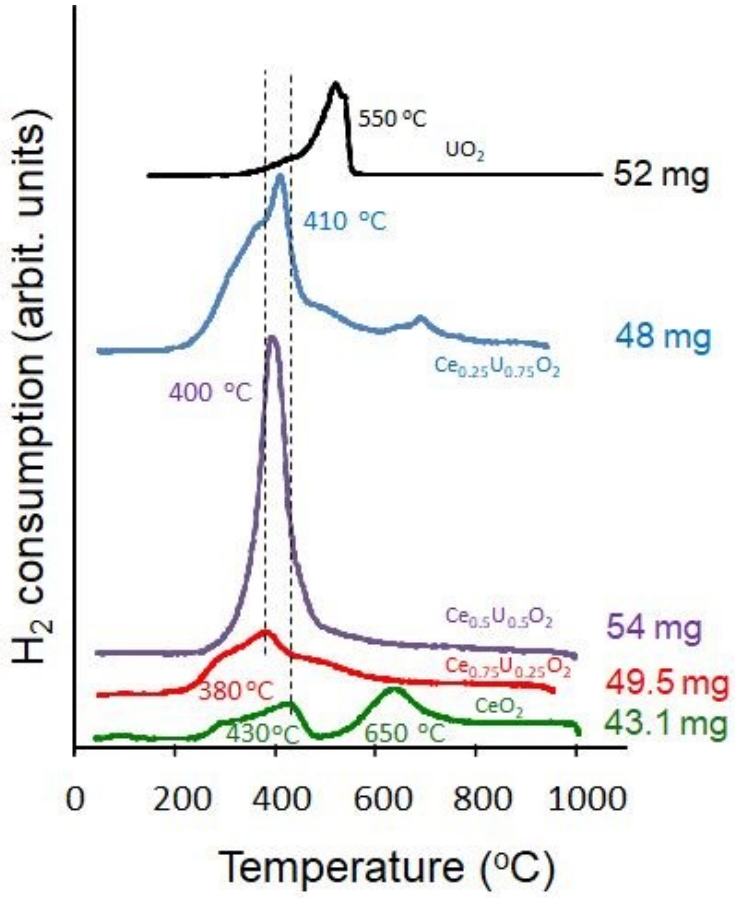

Figure 5.

TPR of a series of $Ce_{1-y}U_yO_2$: CeO_2, $Ce_{0.75}U_{0.25}O_2$, $Ce_{0.5}U_{0.5}O_2$, $Ce_{0.25}U_{0.75}O_2$ and UO_2; ramping rate (10 °C/min). The weight used in each run is indicated on the right-hand side of the curves. Adapted from Ref. [63], permission License number 6133100874303.

Table 4.

Amount of H_2 consumed and the corresponding computed % of lattice oxygen removed from TPR results (assuming that the as -prepared material has the given stoichiometry).

Oxide	Amount of H_2 consumed mL/g_{oxide}	% of removed O atoms	BET surface area m^2/g_{oxide}
CeO_2	24.3	9	71
$Ce_{0.75}U_{0.25}O_2$	21.8	10	33
$Ce_{0.5}U_{0.5}O_2$	32.8	16	34
$Ce_{0.25}U_{0.75}O_2$	38.9	21	30
UO_{2+x}	27.9	excess	17

View Article Online
DOI: 10.1039/D6SE00124F

Figure 5 shows TPR results for a series of $Ce_{1-y}U_yO_2$ oxides. The addition of U cations to CeO_2 resulted in lower reduction temperature and higher hydrogen consumption overall. Because the size of U^{4+} is very close to that Ce^{4+} the increase in reduction is not due to lattice compensation but most likely due to the presence of U cations in higher oxidation state than +4 in addition to possible charge transfer. **Table 4** shows a summary of the H_2 consumption of the series, together with BET surface areas and the calculated fraction of oxygen removed. The addition of U cations further increases the reduction of CeO_2 (from 9 % for CeO_2 alone to 26 % of oxygen atoms removed in the case of $Ce_{0.25}U_{0.75}O_2$). There is also a decrease of the "overall" reduction temperatures when compared to CeO_2 or UO_2 alone. The case of the 0.5 fraction of each cation is intriguing as it presents one single large reduction peak; this however was not further investigated.

Next, TPR of $Ce_{1-y}Fe_yO_2$ together with that of Fe_2O_3 is presented, **figure 6**. The four profiles are plotted as monitored without multiplication and with offset for clarity. The weight of the oxide used is given on the left side of each profile and the total amount of consumed hydrogen is given on the right side. The stoichiometry of the oxides, based on their formulae units, is given next to each line. The table in the inset presents the stoichiometry based on hydrogen consumption (loss of oxygen). Fe_2O_3 is expected to be completely reduced to metallic iron. The needed amount of hydrogen to reduce it (ca. 420 mL/g) is about 80% of that observed ($Fe_2O_3 + 3\ H_2 \rightarrow 2\ Fe + 3\ H_2O$); it may indicate experimental errors of 20% or so but can also, partly be due to excess oxygen (of surface hydroxyls from adsorbed water).

The results of the mixed oxides can be qualitatively explained based on those obtained from the pure ones. The two peaks of CeO_2 labeled I and II may represent surface and bulk reductions. These are qualitatively similar to those reported in **figure 5**, although it is from a different sample batch. Based on XRD (and TEM) results the addition of Fe cations to CeO_2 is substitutional and resulted in decreasing the crystallite size. The decrease in crystallite size would in turn results in increasing the surface to bulk ratio which explains the increase in peak I compared to peak II ratio in the CeFe oxides. Peak III is that of pure Fe_2O_3; because it is also present in the case of $Ce_{0.75}Fe_{0.25}O_{2-\delta}$ some Fe cations may have segregated out of the fluorite structure. The increase in peak II of $Ce_{1-y}U_yO_2$ oxides compared to CeO_2 alone might be due to the ease of bulk reduction due to the presence of Fe cations inside the fluorite structure.

View Article Online
DOI: 10.1039/D6SE00124F

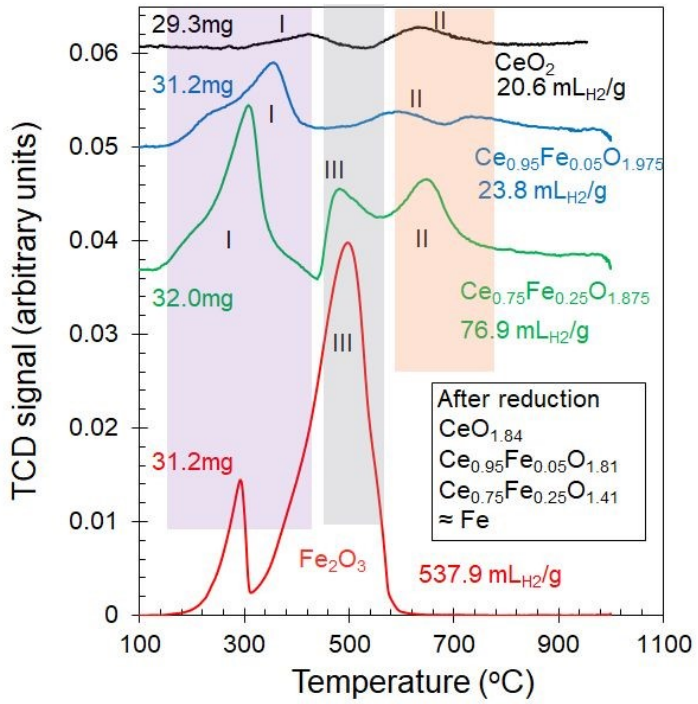

Figure 6.

TPR of CeO_2, $Ce_{0.95}Fe_{0.05}O_{2-\delta}$, $Ce_{0.75}Fe_{0.25}O_{2-\delta}$, and Fe_2O_3. All oxides were pre-calcined at 500ºC. The computed values of 2-δ are given beside each line in the formulae units. The inset rectangle has the computed formulae units based on the oxygen loss during TPR. The amount of hydrogen used to fully reduce Fe_2O_3 to Fe may give an indication on the errors, about 20%. The highlighted regions I and II are those of surface and bulk reduction of CeO_2 while region III is that of bulk reduction of Fe_2O_3. The first peak in the TPR of Fe_2O_3 might be due to surface reduction. From Ref. [50], permission License number 6133081449846

The increased reduction of CeO_2 using Fe was studied by Temperature Programmed Reduction (TPR) in other works. Pure CeO_2 was seen to be reduced in two temperature domains at about 773 K and 1073 K [63]. The first has been attributed to surface reduction while the second to bulk reduction. The reduction is mild (leads to the removal of a small fraction of oxygen anions typically 10-20%) and the formation of Ce^{3+} cations within the investigated temperatures in TPR (typically up to 1273 K). Only few Thermo-Gravimetric Analysis (TGA) experiments of doped CeO_2 with Fe cations are available. In a one particular study devoted to the effect of doping CeO_2 with metal cations, it was found that the incorporation of Fe^{3+} increased the mass loss of CeO_2 (due to reduction). In this case for $Ce_{0.9}Fe_{0.1}O_{2-\delta}$, 50.0 μmol of $O_2/g_{material}$ were removed at each cycle during ten thermochemical cycles in which the thermal reduction step was performed at 1673 K. These were active sites since nearly stoichiometric CO production (by CO_2 reduction) 96.3 $\mu mol/g_{material}$·cycle at 1273 K was seen [64].

View Article Online
DOI: 10.1039/D6SE00124F

4. Valence band ($Ce_{1-y}Fe_yO_2$)

Figure 7 A, B presents the valence band and shallow core levels (Ce5p, O2s, and Ce5s) of $Ce_{0.75}Fe_{0.25}O_{2-\delta}$ and $Ce_{0.95}Fe_{0.05}O_{2-\delta}$ before and after argon ion sputtering for reduction. This reduction method has advantages and disadvantages when compared to reduction in the presence of H_2 or thermally in inert environment. Thermal reduction of these oxides requires heating to at least 1773 K. The mixed oxide at this temperature largely segregates, and therefore, the analysis may not be conducted. Reduction using H_2 in UHV is not possible because of its very low sticking coefficient on oxides. Argon ion sputtering to reduce oxides relies on the mass difference between M and O and the stability of the reduced phase. Ce^{3+}, $Fe^{2+,}$ and Fe^0 are stable in UHV conditions for a few hours because of the low H_2O and O_2 partial pressures. One of the disadvantages of Ar ion sputtering is the loss of surface structure (the formation of an amorphous layer due to the high energy used, 1 kV).

The spectra of the as-prepared oxides (0 min) are dominated by the O2p, O2s, Ce5p and Ce5s lines, marginal changes are seen between both oxides. There are some, surface hydroxyls (-OH, 3σ) at a binding energy of ca. 10 eV. There is also a minor contribution from reduced Ce cations (Ce4f, Ce^{3+}) and reduced Fe cations (Fe3d, oxidation state < +3), both have lower binding energies (at 0.5–2 eV with respect to F_E) than that of the O2p binding energy band.

Upon argon ions sputtering, one notices the following:
(i) An increase of the signal below the O2p line due to reductions (due to increased concentrations of Ce^{3+} and Fe^{+x}, x < +3).
(ii) An increase in surface hydroxyls.
(iii) A relative increase in Ce5p signal with respect to the O2s signal.

For (i) the increase is expected and is treated in more detail to extract quantitative information below. For (ii) the increase, that has been seen before, is due to the increase in the sticking coefficient of the traces of dissociatively adsorbed water over a reduced metal oxide when compared to its stoichiometric form. Ions bombardment causes a reduction due to oxygen removal (as atoms), and the remaining two electrons, per oxygen atom removed (V_O), are transferred to Ce^{4+} (and/or Fe^{3+}) to reduce them. The creation of V_Os leads to the preferential dissociative adsorption of H_2O. This results in the formation of two pairs of surface hydroxyls for each oxygen vacancy healed.

View Article Online
DOI: 10.1039/D6SE00124F

For (iii), this observation is treated qualitatively below.

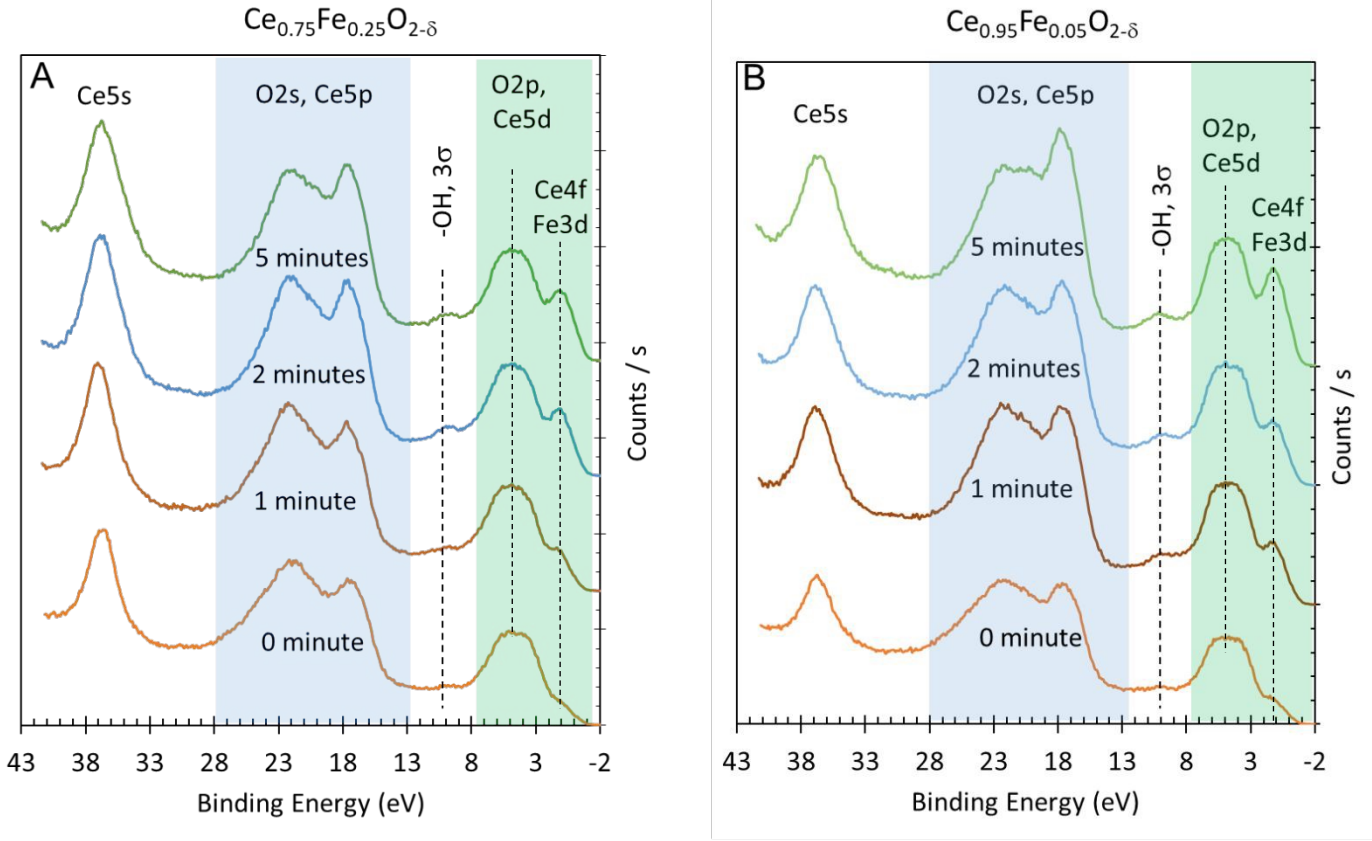

Figure 7.

(**A**) Valence band XPS (green shaded) and Ce5p, O2s (blue-shaded) and Ce5s spectra of $Ce_{0.75}Fe_{0.25}O_{2-\delta}$ before (0 minute) and after argon ion sputtering (x minutes). (**B**) Valence band XPS (green shaded) and Ce5p, O2s (blue-shaded) and Ce5s spectra of $Ce_{0.95}Fe_{0.05}O_{2-\delta}$ before (0 min) and after argon ion sputtering (x minutes). From ref. 16 (no permission is needed: Creative Commons Attribution 4.0 License)

Figure 8 A, B presents the valence band region, in which the signal below the XPS O2p line was fitted by two peaks: at about 0.4 eV and at ca. 1.5 eV, binding energy. There are no noticeable changes in the large O2p lines' shapes upon reduction. For both oxides, the signal attributed to the $Ce4f^1$ orbital is larger than that of the Fe3d orbitals and is more pronounced for $Ce_{0.25}Fe_{0.05}O_{2-\delta}$ when compared to $Ce_{0.75}Fe_{0.25}O_{2-\delta}$. This is consistent with core levels measurements and with the TCWS results (see below). For $Ce_{0.95}Fe_{0.05}O_{2-\delta}$, increasing the reduction time affects mostly the Ce cations, while for $Ce_{0.75}Fe_{0.25}O_{2-\delta}$, it favors Fe reduction. This might be due to the probability of hitting the atoms during bombardment. At a high Fe %, the probability of oxygen removal adjacent to Fe atoms is high, and

View Article Online
DOI: 10.1039/D6SE00124F

therefore more Fe is reduced, while at a low Fe %, the oxide is more homogeneous and the chemical effect on the reduction is expected to be higher.

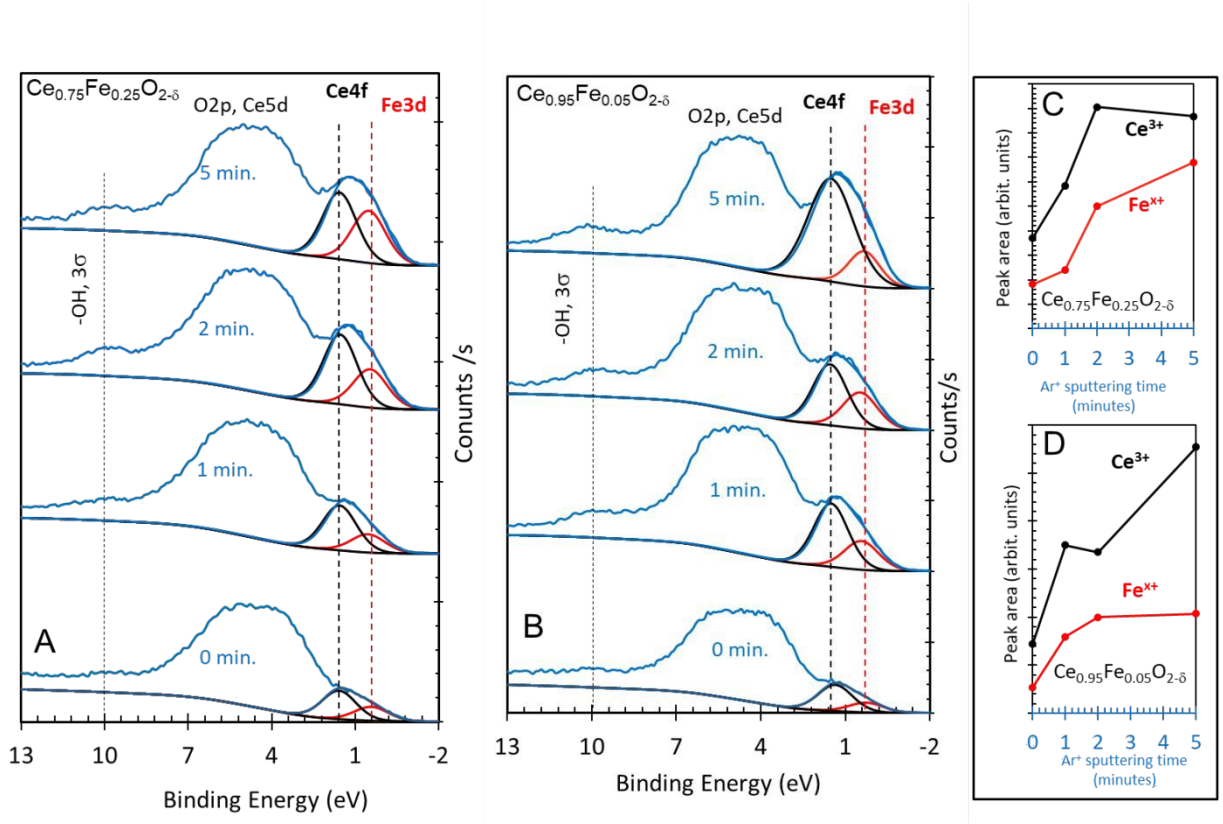

Figure 8.

(**A**) Valence band XPS of as-prepared $Ce_{0.75}Fe_{0.25}O_{2-\delta}$ after 1, 2 and 5 minutes of Ar ion sputtering. (**B**) Valence band XPS of as-prepared $Ce_{0.95}Fe_{0.05}O_{2-\delta}$ after 1, 2 and 5 minutes of Ar ion sputtering. (**C**,**D**) Computed peak areas of fitted Ce4f (FWHM = 1.5 eV) and Fe3d (FWHM = 1.5 eV) signals. From ref. 16 (no permission is needed: Creative Commons Attribution 4.0 License)

Figure 9 A,B presents the valence band and the Ce5p and O2s lines. The spectra are baseline-subtracted, then normalized to highlight the differences. Ions sputtering results in a preferential increase in the Ce5p signal when compared to the O2s lines. In addition, the O2s line becomes narrower. There is no noticeable shift in the binding energy before or after ion bombardment. Similar experiments were conducted on CeO_2, and no change was seen. Some qualitative information may be drawn upon comparisons with previous work conducted by others. In one study also using ions bombardment [65] of CeO_2, (Figure 3a,b of ref. [65]) the relative ratio has increased in favor of the Ce5p orbital, like in this work. The exact position of the O2s orbital with respect to the $Ce5p_{1/2}$ orbital is not clear. Here, it is put after the $Ce5p_{1/2}$ lines similar to other work, although others have put it in between the $Ce5p_{3/2}$ and $Ce5p_{1/2}$ energy positions based on the relativistic computation of CeO_8 and $Ce_{63}O_{216}$ clusters [66]. The

View Article Online
DOI: 10.1039/D6SE00124F

O2s and Ce5p lines give information on charge transfer; because of their quasi-degenerate energy positions they are sensitive to the oxidation state of Ce cations. The spectra in **figure 9** are similar to those reported for a thin film of CeO_2 grown on Rh(111) excited with photon energy equal to 125 eV (Ce4d-Ce4f resonance) [67]. The spectra are also similar to those of irradiated (with Xe ions) CeO_2 thin film and bulk [ref. 65]. The authors pointed out to the final state effect ($3d^94f^1OVMO^{-1}$ (outer valence molecular orbital, OVMO) and $3d^95p^5np^1$ (inner valence molecular orbital, INVO)). The Ce5p atomic orbitals participate in the formation of both OVMO and IVMO, where a large part of the latter is taken by the filled $Ce5p_{1/2}$, $5p_{3/2}$ and O2s atomic shells [68].

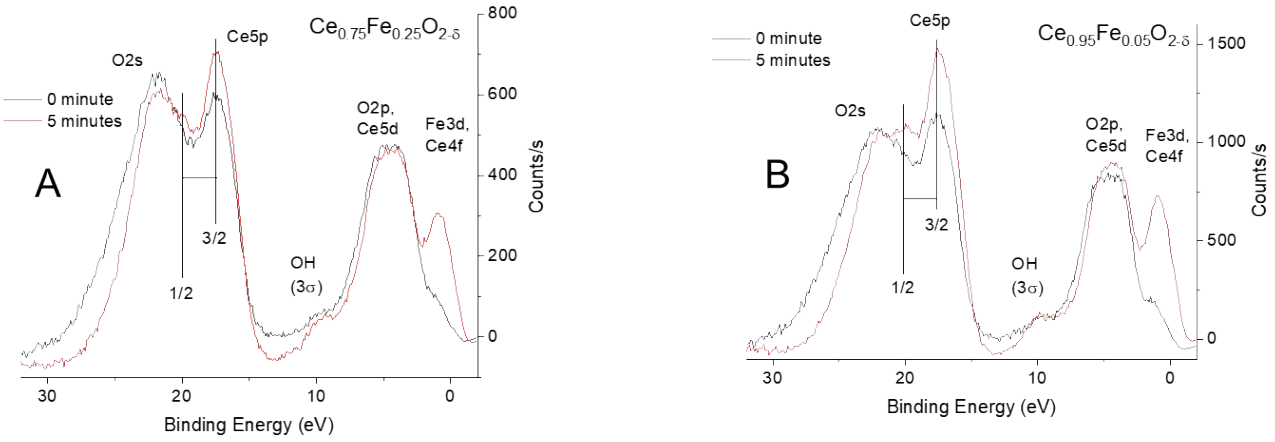

Figure 9.

(**A**) Normalized valence band XPS and the Ce5p and O2s spectra of $Ce_{0.75}Fe_{0.25}O_{2-\delta}$ before (0 minute) and after 5 minutes of argon ion sputtering. (**B**) Normalized valence band XPS and the Ce5p and O2s spectra of $Ce_{0.95}Fe_{0.05}O_{2-\delta}$ before (0 minute) and after 5 minutes of argon ion sputtering. Note the change in intensity of the Ce5p signal when compared to the O2s signal.

The increase in the Ce5p/O2s intensity ratio after sputtering reflects the creation of oxygen vacancies and the associated reduction of Ce^{4+} to Ce^{3+}. Removal of oxygen decreases the O2s contribution to the inner valence molecular orbitals while electrons left by the vacancy populate Ce 4f states. The resulting modification of the Ce–O valence manifold enhances the Ce-derived component of the IVMO. From ref. 16 (no permission is needed: Creative Commons Attribution 4.0 License)

View Article Online
DOI: 10.1039/D6SE00124F

6. X-ray Photoelectron Spectroscopy (XPS) ($Ce_{1-y}Fe_yO_2$)

Figure 10 presents XPS Ce3d lines of Ce cations in the fresh and reduced samples. The presence of both oxidation states of Ce cations is clear. The lines' positions and attributions are shown ($3d_{5/2}$: u, u″ and u‴, and $3d_{3/2}$: v, v″ and v‴ for Ce^{4+} cations, and $3d_{5/2}$: u_o and u′ and $3d_{3/2}$: v_o and v′ for Ce^{3+} cations). In **figure 10** and the inset table, a comparison between the fresh and the most reduced samples is made. The presence of Fe at a 5% concentration resulted in a more pronounced Ce^{3+} concentration when compared to the presence of Fe at a 25% concentration. This is in line with the valence band results presented in **figures 7** and **8**. CeO_2 alone showed a very mild increase upon reduction; this is also in line with the virtually no change in the Ce5p/O2s lines. While Ar ions sputtering relies on momentum transfer of incoming ions (in this case, 1 keV of kinetic energy), which results in breaking the chemical bonds there should be no difference between CeO_2 and Fe-substituted CeO_2 since the incoming ions have much more energy than the chemical bond, assuming complete energy transfer. However, this is a cascade reaction where the energy transfer occurs consecutively, and therefore the last steps of an incoming ion (before it leaves the material or is implanted in it irreversibly) would be more efficient for weaker bonding.

Based on the Ce4f/O2p, Ce5p/O2s and Ce3d (for Ce^{4+} and Ce^{3+}) XPS signals, **Table 5** is made to provide an estimate of the reduction of Ce cations.

View Article Online
DOI: 10.1039/D6SE00124F

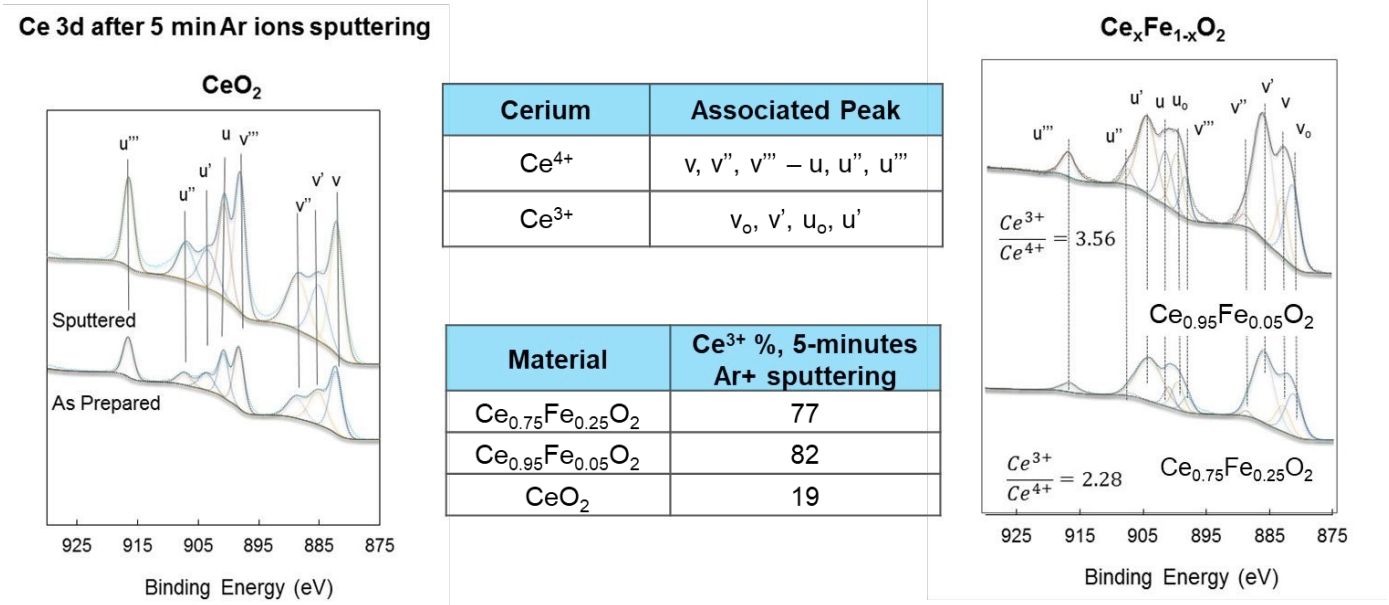

Figure 10.

XPS Ce3d spectra of CeO_2 (left panel), $Ce_{0.75}Fe_{0.25}O_{2-\delta}$ and $Ce_{0.95}Fe_{0.05}O_{2-\delta}$ (right panel) after 5 minutes of Ar ion sputtering. Also shown are the computed contributions of the Ce^{3+} cations. From ref. 16 (no permission is needed: Creative Commons Attribution 4.0 License)

Table 5.

Quantitative values obtained from XPS Ce3d, Ce4f, Ce5p and Fe2p lines. The XPS data are those for reduced oxides after 5 minutes of Ar ions sputtering.

Oxide	Ce^{3+}/Ce^{4+} (Ce3d)	[Ce4f + Fe3d^x]/O2p	Fe^0/Fe^{3+} (Fe2p)	Ce5p/O2s
CeO_2	0.2	≈ 0	≈ 0	1.1
$Ce_{0.75}Fe_{0.25}O_{2-\delta}$	2.3	0.3	0.5	1.6
$Ce_{0.95}Fe_{0.05}O_{2-\delta}$	3.6	0.4	0.6	1.75

View Article Online
DOI: 10.1039/D6SE00124F

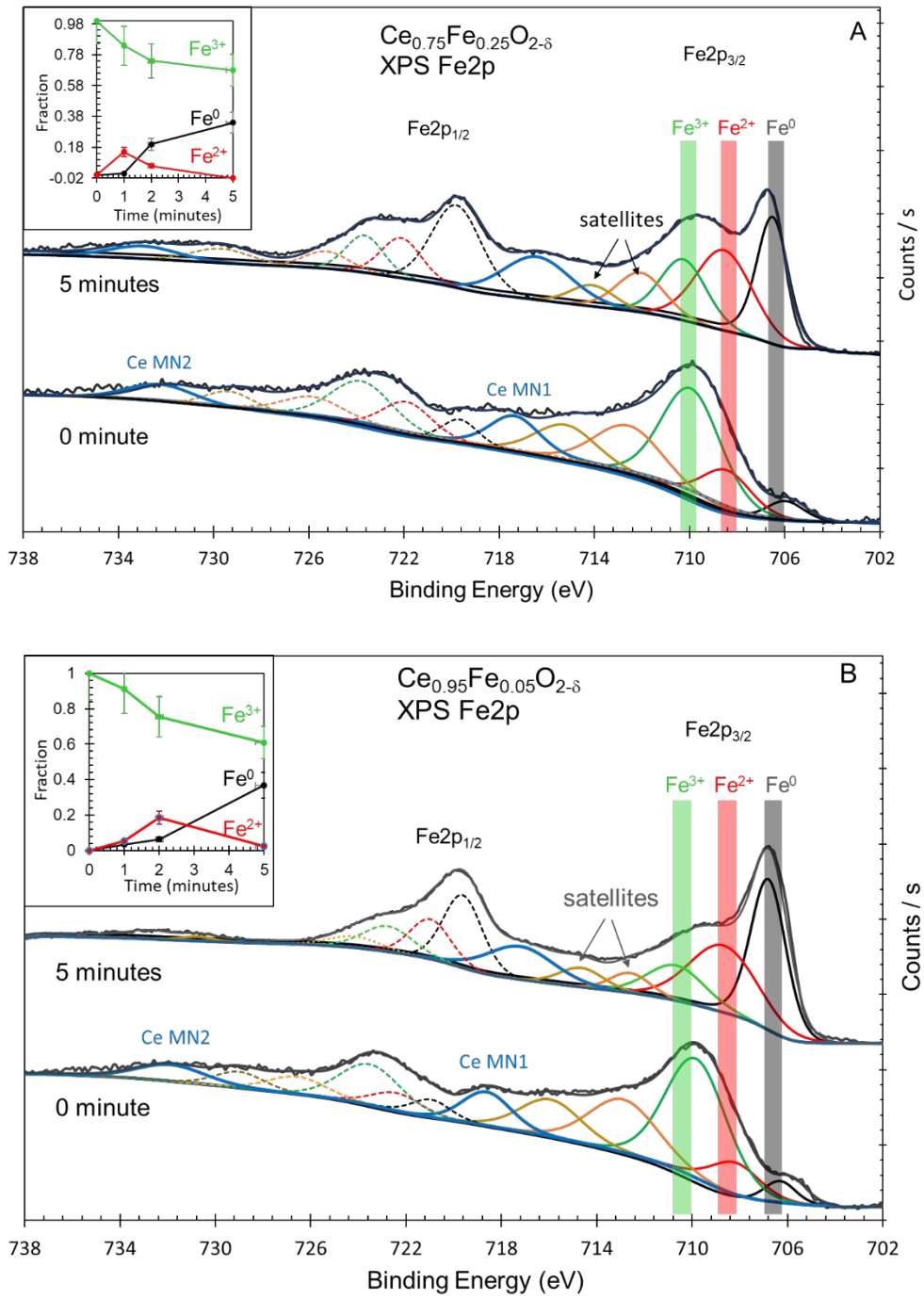

Figure 11.

(**A**) XPS Fe2p spectra of as-prepared $Ce_{0.75}Fe_{0.25}O_{2-\delta}$ after 5 minutes of Ar ions sputtering. (**B**) XPS Fe2p spectra of as-prepared $Ce_{0.95}Fe_{0.05}O_{2-\delta}$ after 5 minutes of Ar ions sputtering. Insets in (**A**,**B**): quantitative analysis of XPS Fe2p spectra of $Ce_{0.75}Fe_{0.25}O_{2-\delta}$ and $Ce_{0.95}Fe_{0.05}O_{2-\delta}$ before and after sputtering at the indicated time. Data acquisitions were conducted using an Al K_α X-rays. From ref. 16 (no permission is needed: Creative Commons Attribution 4.0 License)

View Article Online
DOI: 10.1039/D6SE00124F

The XPS core levels of iron oxides are among the most studied of oxide materials [69]. There are three common oxidation states: Fe^{3+}, such as in Fe_2O_3, Fe^{2+}, such as in FeO, and Fe_3O_4, in addition to Fe^0. The spectra are complicated by the presence of satellites [70,71,72], iron hydroxide (FeOOH) [73,74] and many multiplets [75]. The binding energy of the XPS Fe2p signal is about 707 eV for Fe^0, 710 eV for Fe^{2+} and 711 eV for Fe^{3+}. In $Ce_{1-y}Fe_yO_2$, a further complication arises from the presence of Ce Auger lines in the Fe2p region. Although charge neutralization was used to acquire the spectra, the as-prepared oxide always had wider peaks when compared to that reduced upon ion sputtering. Therefore, peak areas are to be taken as an estimate and binding energies within a 0.5 eV accuracy. Both oxides show similar spectra and trends upon reduction. While, the as-prepared oxides contained Fe^{3+} cations, they, however, also contained Fe^{2+} and some Fe^0. The small % of Fe^{2+} might be formed during the preparation. The presence of metallic iron was not expected and might be due to interstitial atoms formed due to strong lattice distortion. It is also possible that this peak is due to another Auger line of Ce cations. The insets in both figures show the trend during the reduction. In both cases, the amount of Fe^{2+} increases, similar to a previous study [76], then decreases to zero, indicating that within the reduction time studied, all reducible Fe^{3+} cations were transformed to Fe^0. In line with the valence band results, it appears that both Ce^{4+} and Fe^{3+} cations are more efficiently reduced when in small amounts ($Fe_{0.05}$), although the difference is not as pronounced.

7. Epitaxy ($Ce_{1-y}U_yO_2$).

Growing the mixed metal oxide as an epitaxial film in a controlled environment allows more accurate studies of the charge transfer process. It also offers an alternative prototype material for the reaction because both heat and mass transfer limitations would be largely removed. Many previous works have shown epitaxial films of CeO_2 on metal single crystals such as Ru(0001)[77,78,79] and Pt(111)[80,81] surfaces. Here the characterization of a series of $Ce_{1-y}U_yO_{2\pm\delta}$ (111) thin films of about 6 nm thick grown on Ru(0001)/Al_2O_3(0001) templates is presented and discussed.

Figure 12 shows the Low Energy Electron Diffraction (LEED) pattern of (111)-oriented epitaxial thin films for a series of $Ce_{1-y}U_yO_{2\pm\delta}$. Samples with low U content present a faint ring associated with a fraction of randomly oriented islands. Increasing the U fraction translates into a blurring of the spots due to a higher disorder and a larger density of structural defects. The absence of Ru(0001) spots indicates a complete coverage of the whole substrate.

View Article Online
DOI: 10.1039/D6SE00124F

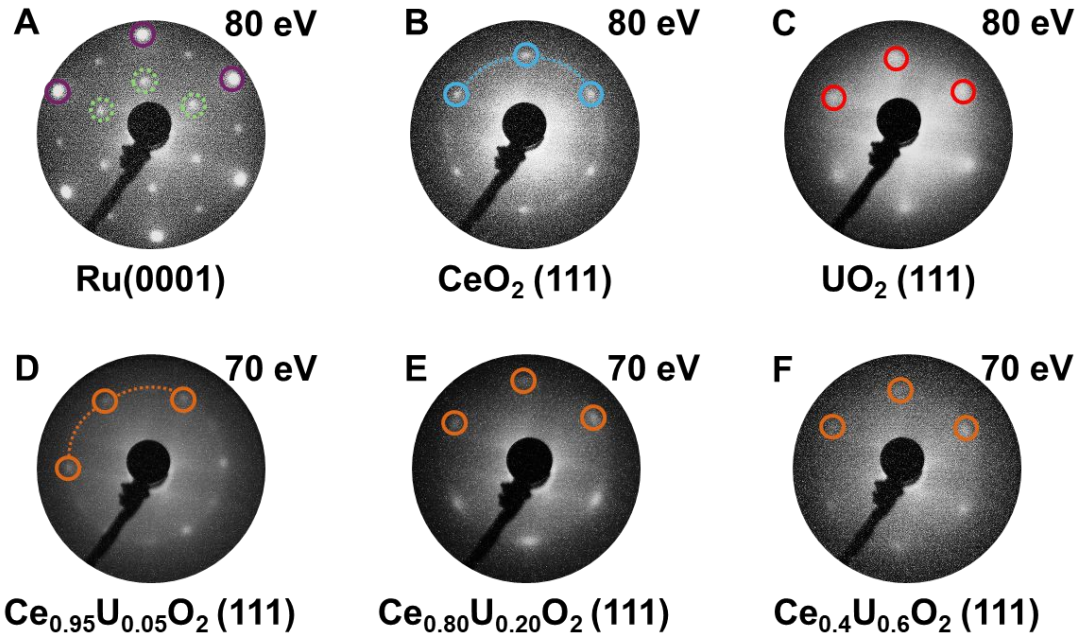

Figure 12.

LEED patterns: **A.** Clean Ru(0001)/Al_2O_3(0001) substrate. The hexagonal pattern indicated by solid violet circles corresponds to the Ru spots, while the dashed green circles indicate the (2x1) reconstruction of adsorbed oxygen. **B.** and **C.**, CeO_2 and UO_2 (111) reference thin films; solid circles (blue and red) indicate their spots in azimuthal registry with the Ru(0001). For the CeO_2 pattern, the dashed blue arc indicates the faint ring associated with a small fraction of randomly oriented islands. **D., E.,** and **F.** LEED patterns of $Ce_{1-y}U_yO_{2\pm\delta}$ thin films with y = 0.05, 0.2, and 0.6, respectively. Solid orange circles indicate their spots in azimuthal registry with the Ru(0001). From ref. 22 (no permission is needed: Creative Commons Attribution 4.0 License).

In situ XPS measurements of Ce3d and U4f regions are presented in **Figure 13** (**A** and **B**) for CeO_2 and UO_2 references, respectively. The Ce 3d lines are dominated by the Ce^{4+} cations (v = 882.6 eV, v'''= 898.7 eV, and u'''= 916.9 eV) for the UHV annealed film. The small contribution from Ce^{3+} cations (v' ca. 886 eV) disappears upon heating in O_2. For the UHV annealed UO_2 film, XP U 4f spectra indicate the presence of U^{4+} cations (U $4f_{7/2}$ = 380.2 eV and its satellite at 6.9 eV above). Heating in the presence of O_2 resulted in the oxidation of a fraction of U^{4+} cations to U^{5+} cations ($U4f_{7/2}$ = 381.1, $U4f_{5/2}$ = 391.8 and its satellite at ca. 8 eV above; the U $4f_{5/2}$ component of the U^{4+} cations obscures the $U4f_{7/2}$ satellite of the U^{5+} cations) [82]. The UHV annealed films are mostly composed of Ce^{4+} (for CeO_2) and exclusively composed of U^{4+} (for UO_2).

View Article Online
DOI: 10.1039/D6SE00124F

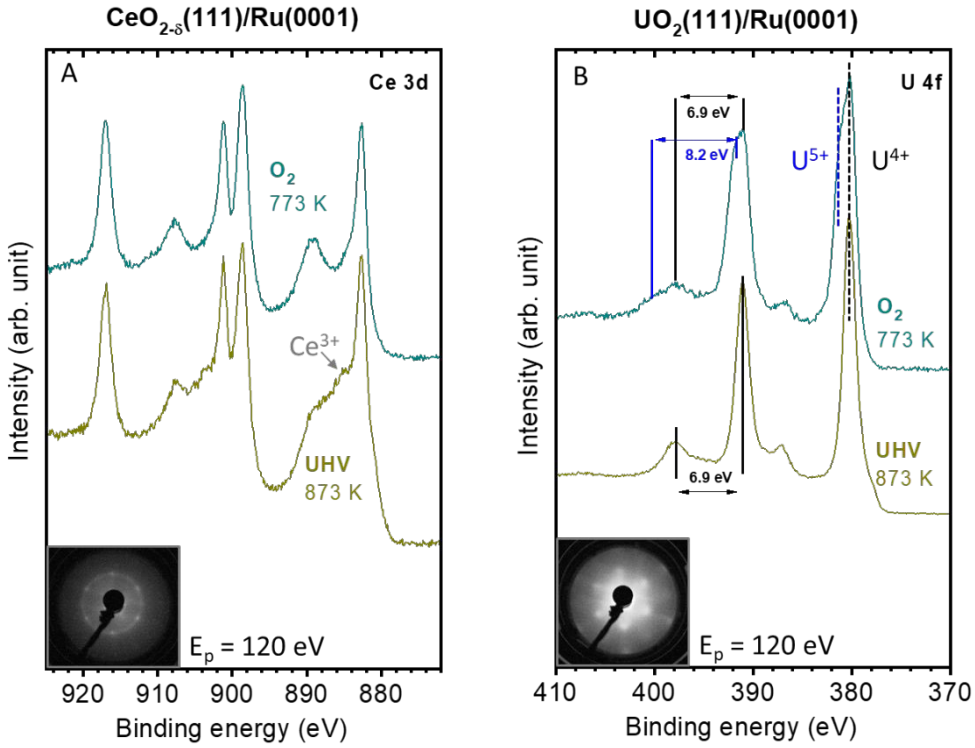

Figure 13.

A. XPS Ce 3d of CeO_2 thin film after annealing in UHV (bottom) and heating in 5 10^{-7} mbar O_2 for 30 minutes (top). **B**. XPS U 4f of UO_2 thin film after annealing in UHV (bottom) and heating in 5 10^{-7} mbar O_2 for 30 minutes (top). The insets show the LEED images of the UHV annealed films. From ref. 22 (no permission is needed: Creative Commons Attribution 4.0 License).

8. Charge transfer from U^{4+} to Ce^{4+} cations

8.a. Experimental

A noticeable difference is seen for the mixed oxides samples. **Figure 14** (**A** and **B**) presents the same XPS regions as those shown in **Figure 13** for the $Ce_{0.8}U_{0.2}O_{2\pm\delta}$. XPS Ce 3d indicates (**Figure 14 A**) that the UHV annealed film contains a significant fraction of Ce^{3+} (which was not observed for $CeO_{2\pm\delta}$); the estimated ratio Ce^{3+}/Ce^{4+} is equal to 2.7. XPS U 4f lines of the same film contain a large fraction of U^{5+} (the UHV annealed of UO_2 did not contain U^{5+}); the U^{5+}/U^{4+} was found equal to 1.5. Similar trends were obtained for other investigated mixed oxides, yet quantitative differences were observed. In particular, the charge transfer occurs during the annealing process (as indicated by **equation 3**). Heating in O_2 resulted in preferential oxidation back to Ce^{4+}, yet under these conditions, part of the oxygen consumed for the oxidation was taken or transferred from U^{5+}-O because the oxidation trend has reversed (**Figure**

View Article Online
DOI: 10.1039/D6SE00124F

14 B). This indicates that the dynamic of the electron transfer between both metal cations is sensitive to the partial pressure of O_2 in addition to the Ce to U ratio.

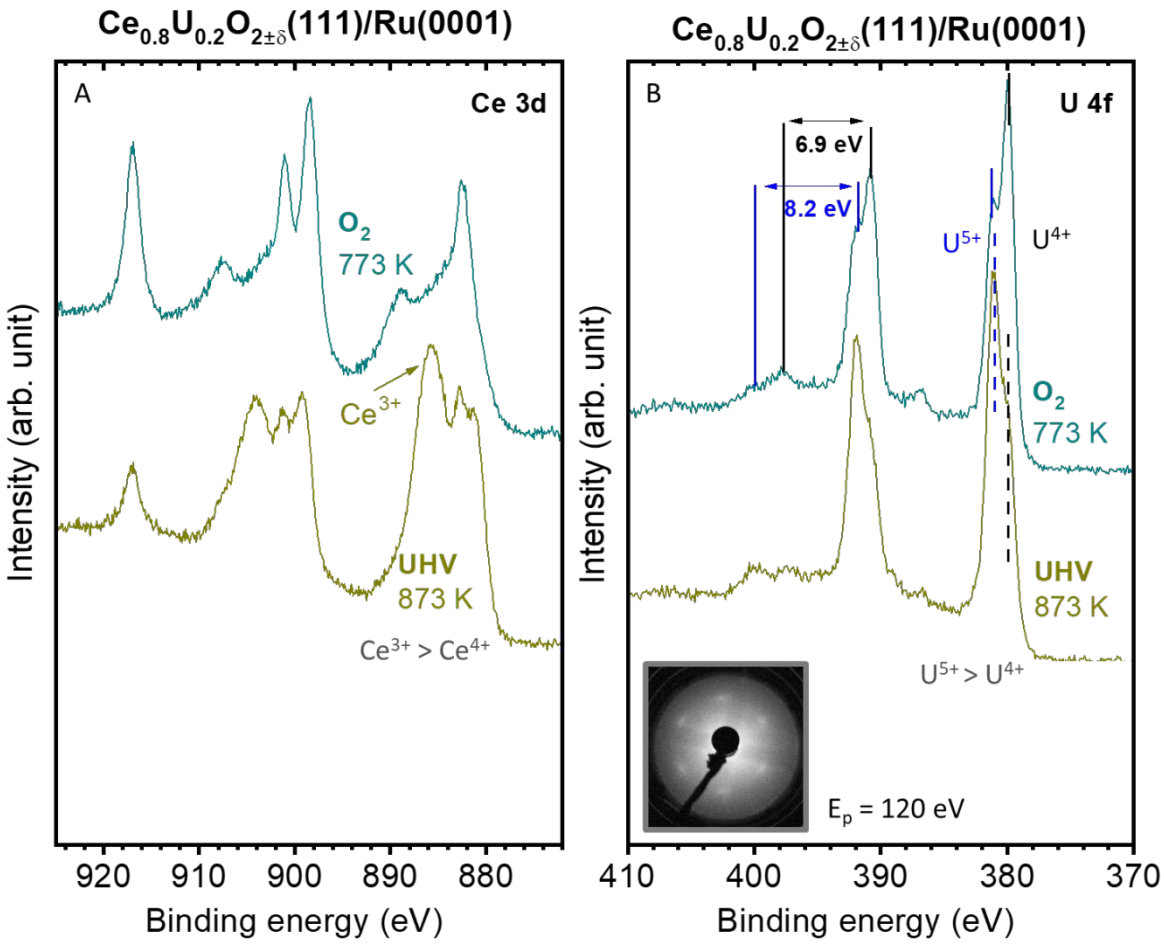

Figure 14.

A. XPS Ce3d of $Ce_{0.8}U_{0.2}O_{2\pm\delta}$ after annealing in UHV (bottom) and heating in 5 10^{-7} mbar O_2 for 30 minutes (top). **B.** XPS U4f of $Ce_{0.8}U_{0.2}O_{2\pm\delta}$ after annealing in UHV (bottom) and heating in 5 10^{-7} mbar O_2 for 30 minutes (top). The inset shows the LEED images of the UHV annealed samples. The arrows in B. point to the ΔE of the satellites (6.9 eV for $U4^+$ and 8.2 eV for U^{5+}). From ref. 22 (no permission is needed: Creative Commons Attribution 4.0 License).

View Article Online
DOI: 10.1039/D6SE00124F

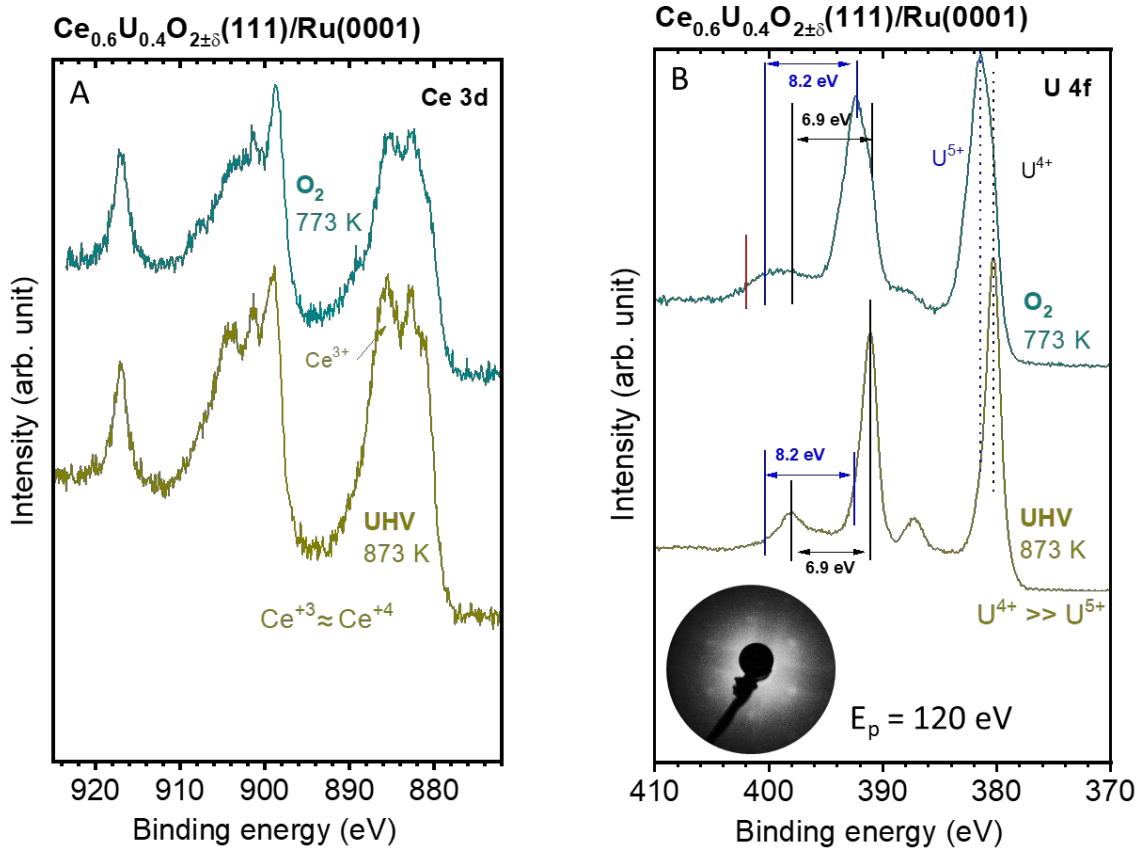

Figure 15.

A. XPS Ce 3d of $Ce_{0.4}U_{0.6}O_{2\pm\delta}$ after annealing in UHV (bottom) and heating in 5 10^{-7} mbar O_2 for 30 minutes (top). **B.** XPS U 4f of $Ce_{0.4}U_{0.6}O_{2\pm\delta}$ after annealing in UHV (bottom) and heating in 5 10^{-7} mbar O_2 for 30 minutes (top). The inset shows the LEED image of the UHV annealed sample. The arrows in B. point to the ΔE of the satellites (6.9 eV for $U4^+$ and 8.2 eV for U^{5+}). The red line is at the position of a U^{6+} satellite; this, together with the large FWHM of the main lines ($U4f_{7/2,5/2}$), indicates that U cations have a wide range of oxidation states from +4 to +6. From ref. 22 (no permission is needed: Creative Commons Attribution 4.0 License).

8.b. Compositional effect ($Ce_{1-y}U_yO_2$).

Increasing the percentage of U decreased the fraction of oxidized U cations **Figure 15** (**A** and **B**). Also, the ratio Ce^{3+}/Ce^{4+} decreased compared to that of the lower U content. This trend indicates that the reduction of Ce^{4+} decreases when U cations content is significant and is not solely explained by the charge transfer described in **equation 3**. However, Ce^{3+} cations were still present even when heated in O_2, while U cations were oxidized to U^{5+} and a small fraction to U^{6+}. As mentioned above, previous works on polycrystalline $Ce_{0.5}U_{0.5}O_2$ showed segregation of the uranium oxide upon heating [20], with diffraction lines that are attributed to either/or U_2O_5 and U_3O_8. Taking these observations together and the fact that UO_2 tends to become $UO_{2+x,}$ one may conclude that it may segregate to the top of the thin

View Article Online
DOI: 10.1039/D6SE00124F

film, shielding CeO_2 from being oxidized, and that is why Ce^{3+} cations are still present even when the film was annealed in the presence of O_2. While Ce^{3+} cations are formed, when the percentage of U cations is high, the former will not be as active because they are in deeper layers, thus explaining the decrease of the activity of the mixed oxide for water splitting (as presented below) with increasing U content after the optimal concentration.

8.c. Computation.

Figure 16 (**A** and **B**) presents the results of the DFT+U computation of $Ce_{31}UO_{64}$ before and after creating an oxygen vacancy to make a $Ce_{31}UO_{63}$ super-cell. There are no Ce4f electrons before the removal of the oxygen ion, while three electrons on three Ce cations (Ce4f orbitals) are seen after the creation of the V_O. Removing an oxygen ion from the lattice has resulted in the transfer of two electrons towards two Ce^{4+} cations, plus the additional reduction of a third Ce^{4+} to Ce^{3+} due to charge transfer from U^{4+} that becomes U^{5+}. **Figure 16** (**C** and **D**) presents the bond distances between Ce (U) and oxygen ions and the Bader charge analysis in the presence of V_O. Contraction in the U-O bonds and expansions in the Ce-O bonds is observed. Quantitative description is given in **Table 6,** in which the focus is made on the bonds of seven oxygen anions with Ce and U cations (the oxygen atoms are labeled 1 to 7). Ce^{3+} cations directly adjacent to the vacancy experience an expansion in their bond distance to the nearest oxygen by 2.7 %. Also, Ce^{4+} cations adjacent to the nearest oxygen atoms, labeled $Ce_{d\text{-}i}$, experience an even larger bond distance expansion of 6.7 %. On the contrary, the U^{5+} cation shows a contraction of its bond distances to the seven oxygen ions. The contraction is, anisotropic and spans from 2.5 to 6.6 %.

To study the configurational effect of U cations on the reduction of Ce^{4+} cations, computation of a system in which U cations having the same concentration but in two different positions were conducted. **Figure 17** (**A** and **B**) presents results from a super cell (4 x 2 x 1) containing 3 U cations of a $Ce_{29}U_3O_{64}$. In one case (**figure 17 A**) they are surrounding a Ce^{4+} cation, representing a high local concentration, while in the second case (**figure 17 B**) one of the three cations is moved away, three units to the left on the x-axis and one unit up on the y-axis (a unit is defined as the Ce^{+4} to Ce^{+4} distance, which is equal to 3.86 Å).

View Article Online
DOI: 10.1039/D6SE00124F

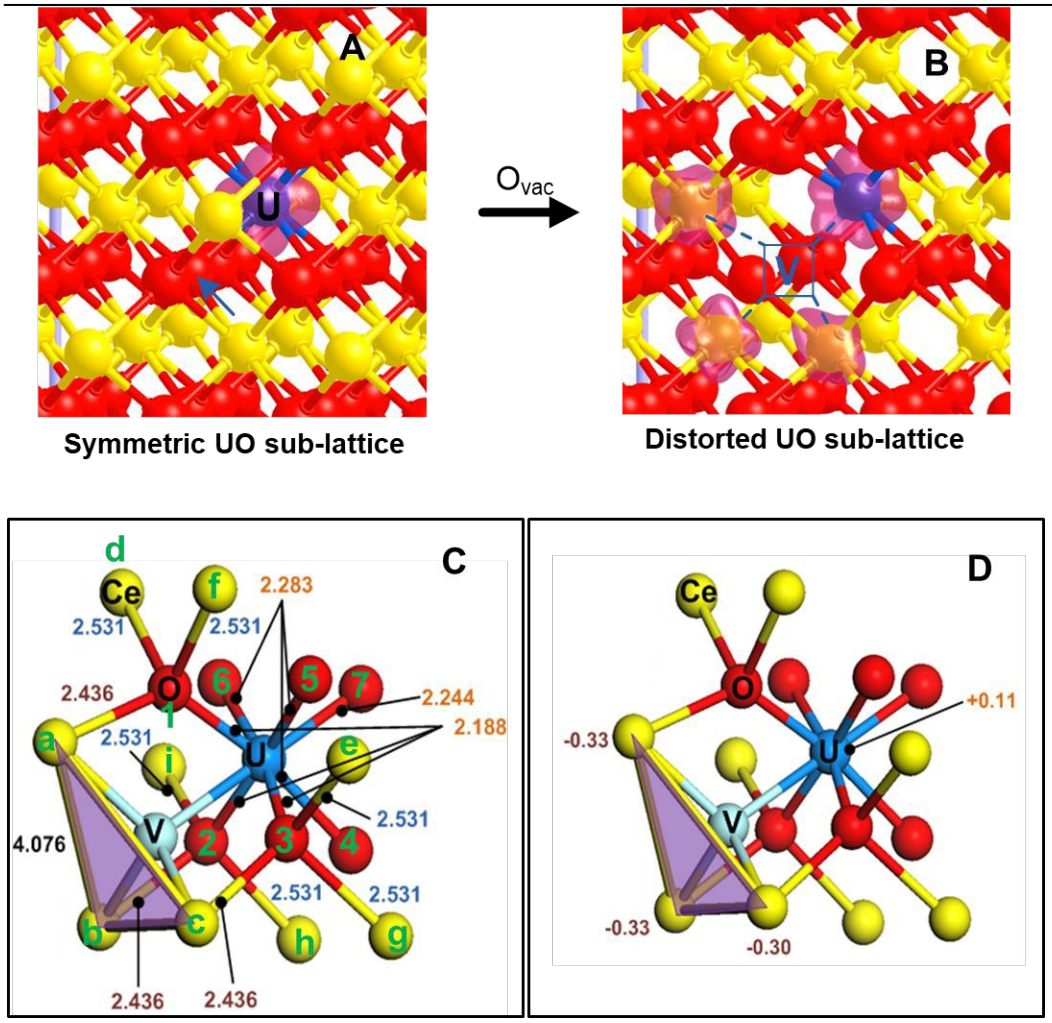

Figure 16.

A. A section of the super cell ($Ce_{1-x}U_xO_2$: (2 x 2 x 2) model (31 Ce, 1 U, and 64 O atoms); U % = 3.1%) showing the U cation (purple), Ce cations (yellow) and oxygen anions (red). The arrow points to the oxygen ion to be removed. Note the 5f orbitals of the U^{4+} cation that contain two electrons and the absence of 4f electrons on the Ce^{4+} cations. **B.** the same section as in A after removing the oxygen anion. Three Ce cations have accommodated one electron each in their 4f states, while the U cation has lost one electron. **C.** Bond distances of the Ce and U cations adjacent to the oxygen vacancy (Ce-O and U-O distances of the stoichiometric cells are Ce-O = 2.372 Å and U-O = 2.342 Å). **D.** Bader charges on the three Ce cations and U cation in the presence of V_O. From ref. 22 (no permission is needed: Creative Commons Attribution 4.0 License).

No electron transfer occurred in the first configuration, while in the second, in which only two U cations were adjacent to Ce^{4+}, transfer did occur to the Ce cation at equidistance from the two U cations. This occurred in the absence of V_O. **Figure 17** (**C** and **D**) presents a specific case of **Figure 17 B**. The removal of an oxygen ion in this case did not result in the formation of three Ce^{3+} but in two. In this case, the presence of the two U cations adjacent to each other prevented the charge transfer upon the removal of an oxygen ion.

View Article Online
DOI: 10.1039/D6SE00124F

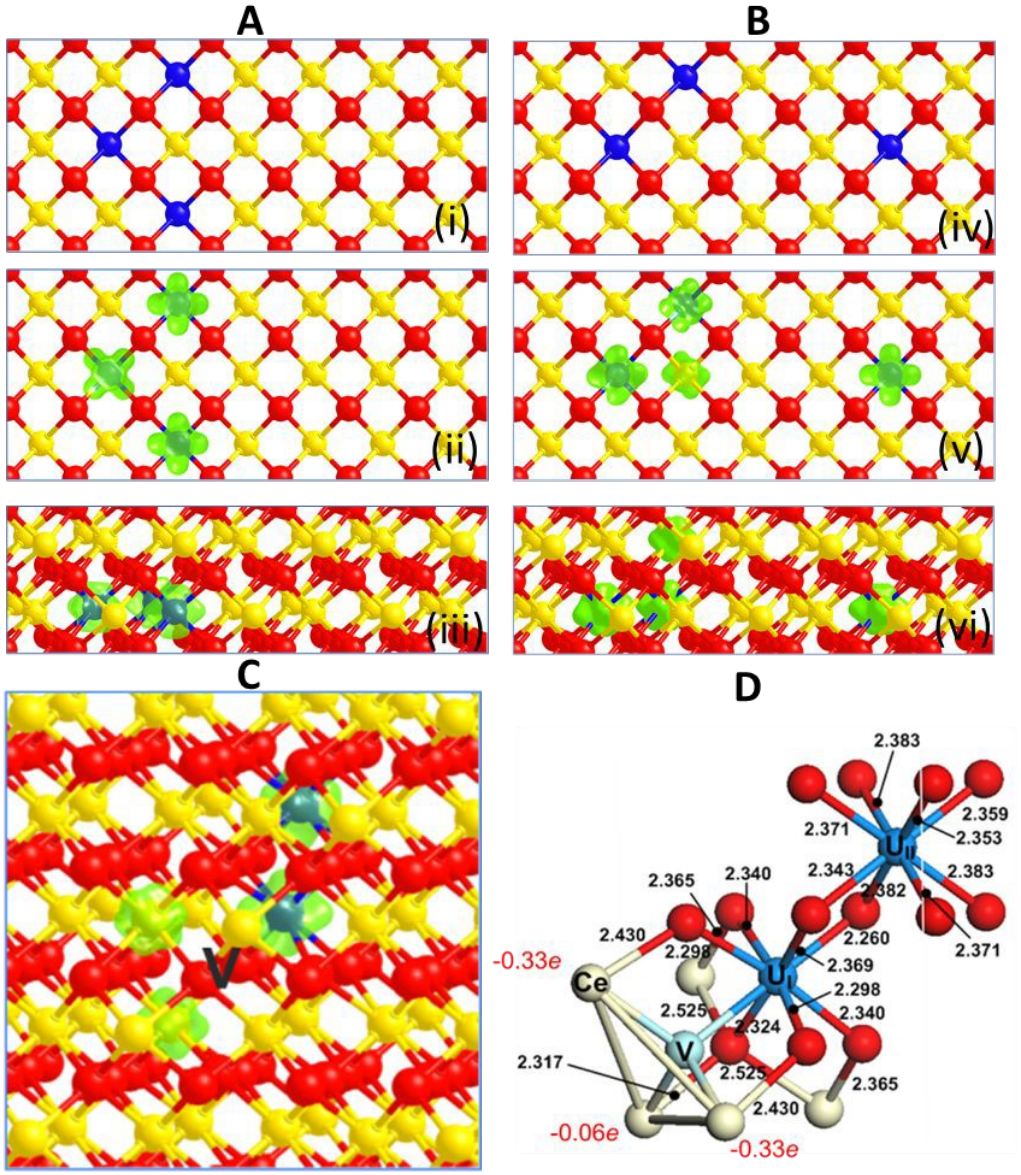

Figure 17.

A. and **B.** Effect of U arrangement around Ce ions on electron transfer. U concentration is 9.3% of the (4 × 2 × 1) bulk model ($Ce_{29}U_3O_{64}$ ($Ce_{0.907}U_{0.093}O_2$)). (i) and (iv) U, Ce, and O are in blue, yellow, and red; top view. (ii) and (v) Projected orbitals on U and Ce ions; top view. (iii) and (vi) Projected orbitals on U and Ce ions; side view. **C.** U concentration is 6.2% of the (2 × 2 × 2) bulk model ($Ce_{30}U_2O_{63}$ ($Ce_{0.937}U_{0.063}O_{1.969}$)) in the presence of V_O. **D.** Bond distances and Bader charge on Ce in the presence of V_O (from **C**). From ref. 22 (no permission is needed: Creative Commons Attribution 4.0 License).

Table 6.

Bond distances between Ce (U) and O ions upon the removal of one O atom from $Ce_{31}UO_{64}$ super cell. The % changes are from the Ce-O and U-O distances of the stoichiometric cell (Ce-O = 2.372 Å and U-O = 2.342 Å). The alphabetical subscripts in Ce and numerical subscripts in O are displayed on the corresponding atoms in Figure 7 in the main text. From ref. 22 (no permission is needed: Creative Commons Attribution 4.0 License).

View Article Online
DOI: 10.1039/D6SE00124F

Atom	$O_{1,2,3}$	$O_{4,5,6}$	O_7
$Ce_{a,b,c}$	2.436 (+2.7%)		
U	2.188 (-6.6 %)	2.283 (-2.5 %)	2.244 (-4.2 %)
$Ce_{d,e,f,g,h,i}$	2.531 (+6.7 %)		

Based on the results on polycrystalline and epitaxial $Ce_{1-y}U_yO_2$ samples, it was observed (in both cases) that charge transfer from U to Ce cations occurs. Its extent, however, has a considerable entropic factor. While low concentrations of U cations are needed, this is not solely related to a dilution effect. Also, the analysis of model $Ce_{1-y}U_yO_2$ (111) thin films indicates that the fraction of Ce^{4+} reduced to Ce^{3+} is larger than that of U^{4+} oxidation to U^{5+} (or U^{6+}) by a factor far exceeding experimental uncertainties (more details can be found in ref. 22). At high U concentrations, U cations migrate to the shell of the crystallites. Besides the fact that UO_2 is easily oxidized to higher oxidation states, O_2 adsorption on UO_2(111) is possible (with a computed adsorption energy of -0.24 eV) [83], whereas there are no known experimental reports of O_2 irreversible adsorption on CeO_2(111). Together, these facts would result in a core-shell structure ($UO_z/Ce_{1-y}U_yO_2$), preventing Ce^{3+} cations from being oxidized in the core of the crystallite. Such element migration and phase separation are not uncommon in metallic nanoparticles; for example, an alloy of RhPd or RhPt particles sees migration of Rh to the surface in an oxidized environment [84] because it is easier to oxidize Rh when compared to Pt or Pd. The reduction of Ce cation in the presence of U cations, while occurs through charge transfer, is therefore sensitive to the configuration of the metal cations, and, as pointed out computationally before (ref. 11), its energy is sensitive to statistical entropy contribution.

9. Hydrogen production from water

9.a. Polycrystalline $Ce_{1-y}Fe_yO_2$

Figure 18 presents hydrogen production on CeO_2, $Ce_{0.95}Fe_{0.05}O_{2-\delta}$ and $Ce_{0.75}Fe_{0.25}O_{2-\delta}$ from water, These were prior reduced with hydrogen 973 K (700 ºC). The use of hydrogen allows reduction at temperature low enough were phase segregation is minimal. Moreover, while the TCWS technology relies on direct energy input from the sun using solar concentrators, with its considerable challenges [85], at the laboratory scale heat is provided by electrical furnaces instead in order to maintain a controlled and stable energy source. The objective here is to relate H_2 production (performance) to the observed reduced states (spectroscopy) of the oxides. Because, as indicated by XRD, the two mixed

View Article Online
DOI: 10.1039/D6SE00124F

oxides are not segregated when heated to this temperature, a link to spectroscopic measurements is possible. CeO_2 alone shows negligible activity, while the Fe-substituted cerium oxides are active. The activity of the $Ce_{0.95}Fe_{0.05}O_{2-\delta}$ is almost twice that of the $Ce_{0.75}Fe_{0.25}O_{2-\delta}$ catalyst. This suggests that the activity is more linked to Ce^{3+} than to Fe^0 (based on the XPS Ce3d and XPS Ce5p/O2s spectra).

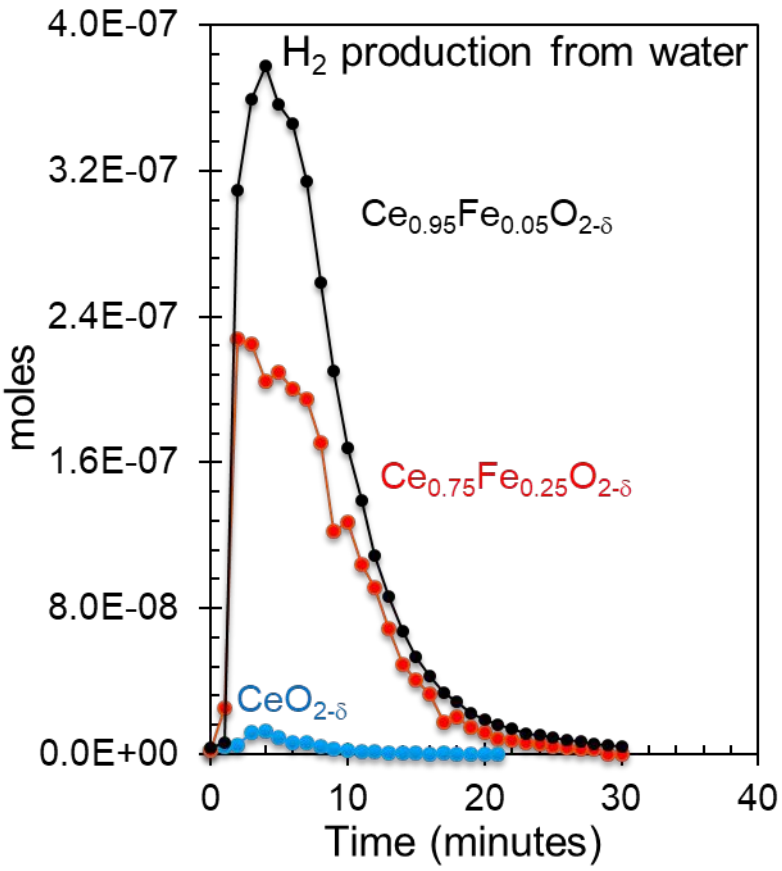

Figure 18.

Hydrogen production from water over CeO_2, $Ce_{0.75}Fe_{0.25}O_{2-\delta}$ and $Ce_{0.95}Fe_{0.05}O_{2-\delta}$, which were previously reduced with hydrogen at 973 K at one atmosphere (reaction temperature = 973 K). The total H_2 production was found equal to 0.2, 7.4 and 11.4 $\mu mol/g_{oxide}$ for CeO_2, $Ce_{0.75}Fe_{0.25}O_{2-\delta}$ and $Ce_{0.95}Fe_{0.05}O_{2-\delta}$, respectively. From ref. 16 (no permission is needed: Creative Commons Attribution 4.0 License)

9.b. Polycrystalline $Ce_{1-y}U_yO_2$

The water splitting to hydrogen at 973 K for the series polycrystalline $Ce_{1-x}U_xO_{2\pm\delta}$ (where $0.05 \leq x \leq 0.75$, including pure CeO_2 and UO_2) was further studied to see the effect of substituting Ce^{4+} by U^{4+} cations on the reaction. **Figure 19 A** presents H_2 production from water (vapor pressure 23 torr) as a function of time over a prior reduced $Ce_{0.95}U_{0.05}O_2$. The calculated total H_2 production per weight over these oxides is presented in **figure 19 B**. The binary oxides (CeO_2 and UO_2) show a small activity at both ends of the plot. The presence of U in small amounts resulted in an enhancement of H_2 production

View Article Online
DOI: 10.1039/D6SE00124F

by ca. 30 times when compared to CeO_2. Increasing the amounts of U, while still showed enhancement compared to CeO_2, was less pronounced. Also presented are the percentage of Ce^{3+} states (as obtained from XPS Ce 3d lines [20] that were produced upon Ar-ions sputtering of the same polycrystalline mixed oxide series. The trend is similar to H_2 production: substituting Ce by U cations increased the reduction of Ce^{3+} considerably. **Figure 19 C** presents some of the data of the H_2 production shown in **figure 19 B** as a function of bulk V_O formation energy (E_{VO}), computed using DFT+U (U_{eff} = 4 eV for U and 5 eV for Ce) taken from ref. [13]. E_{VO} represents the energy required to remove an oxygen atom from the oxide lattice and is defined as the energy difference between a reduced slab and the sum of the energies of the corresponding stoichiometric slab and the removed oxygen atoms. If oxygen vacancies were isolated and non-interacting, one expects a linear relationship between E_{VO} and the extent of reduction δ, taking in consideration that H_2 production is proportional to δ/2 (as per equation 2).

The introduction of U considerably decreased the energy needed to remove bulk oxygen atoms. The effect is offset by increasing U content, because it is harder to reduce U^{4+} cations.

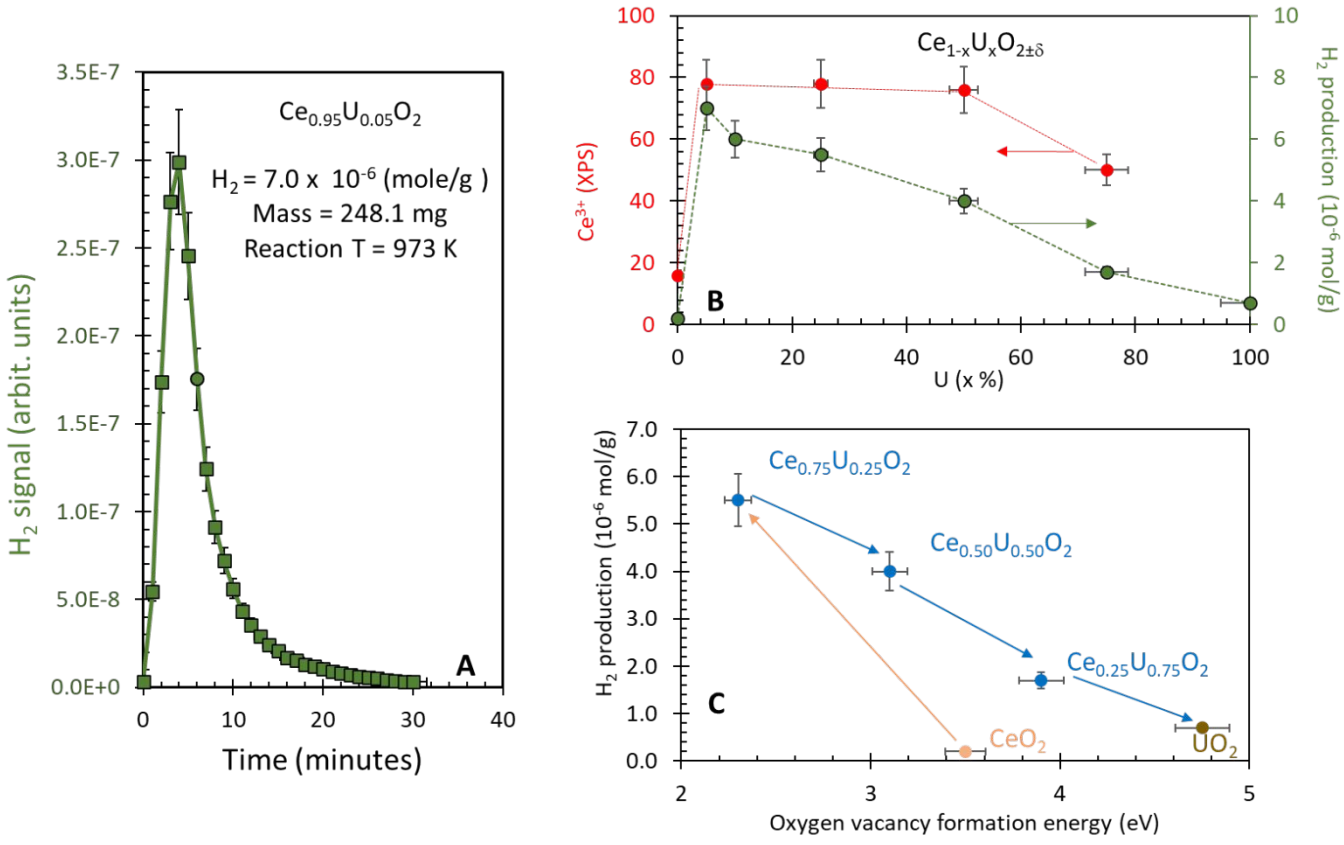

Figure 19.

A. H_2 production from water at 973 K on pre-reduced $Ce_{0.95}U_{0.05}O_2$. **B.** H_2 production on a series of $Ce_{1-x}U_xO_{2\pm\delta}$ mixed oxide as a function of U content (right y-axis). The percentage of Ce^{3+} (XPS Ce3d lines from Ref. [20]) cations obtained upon reduction with Ar-ions prior to XPS collection is shown in the left y-axis. **C.** H_2 production on a selected samples from the series presented in **B** as a function of V_O

View Article Online
DOI: 10.1039/D6SE00124F

formation energy computed using DFT+U, from ref. [12]. From ref. 22 (no permission is needed: Creative Commons Attribution 4.0 License).

10. Thermal water splitting ($Ce_{1-y}Fe_yO_2$)

Figure 20 presents the activity of reduced CeO_2 and reduced $Ce_{0.95}Fe_{0.05}O_{2-\delta}$ for thermal water splitting at 1200°C while **figure 21** presents the STEM, EDX and EELS results of the $Ce_{0.95}Fe_{0.05}O_{2-\delta}$ oxide after the reaction. The reduction was conducted upon heating to 1550°C for two hours in the absence of H_2 (under N_2). The incorporation of Fe (Fe/Ce = 0.05) into CeO_2 has resulted in two main effects. It increased the kinetic of H_2 production (**figure 20 C**) and the yield; total amount has almost doubled (per unit weight of oxide (**figure 20 B** and **C**). This is in line with spectroscopic results where there is an increased reduction of CeO_2 due to the presence of Fe cations (up to a threshold level). The FWHM of the production peak decreased from ca. 35 min to about 10 min which gives a simple observation on the kinetic effect. To further see the effect of Fe on the reduction kinetics, the decay part of the peaks was fitted with an exponential function. Attempts with a single exponential decay fit were not successful, a double exponential fit was found to be adequate with R^2 of 0.999. **Table 7** presents the different parameters of the decay for both oxides. The addition of Fe has increased the time constant for water splitting by a factor of 2 when compared to CeO_2 alone. However, increasing the number of reduced sites, should not change the decay time but mostly affect the amplitude (pre-factors A_1 and A_2) if these sites were all of similar nature and do not interact with each other. The increase of the time constant by a factor of two indicates that the reduced sites are more reactive than those of reduced CeO_2 alone. It is not simple to attribute a separate physical meaning to both decay constants. It is possible that the (t_2) decay describes events requiring more (or additional) energy than the first one; such as defects diffusion from the bulk to the surface. Initially defects are statistically distributed in the bulk and on the surface, then with the reaction progress more available defects are healed (and the process would more dependent on diffusion of O^{2-} (or V_O) within the oxide), and this decreases the reaction rate. In other words, the first decay might be largely independent from defects distribution and migration while the second is.

View Article Online
DOI: 10.1039/D6SE00124F

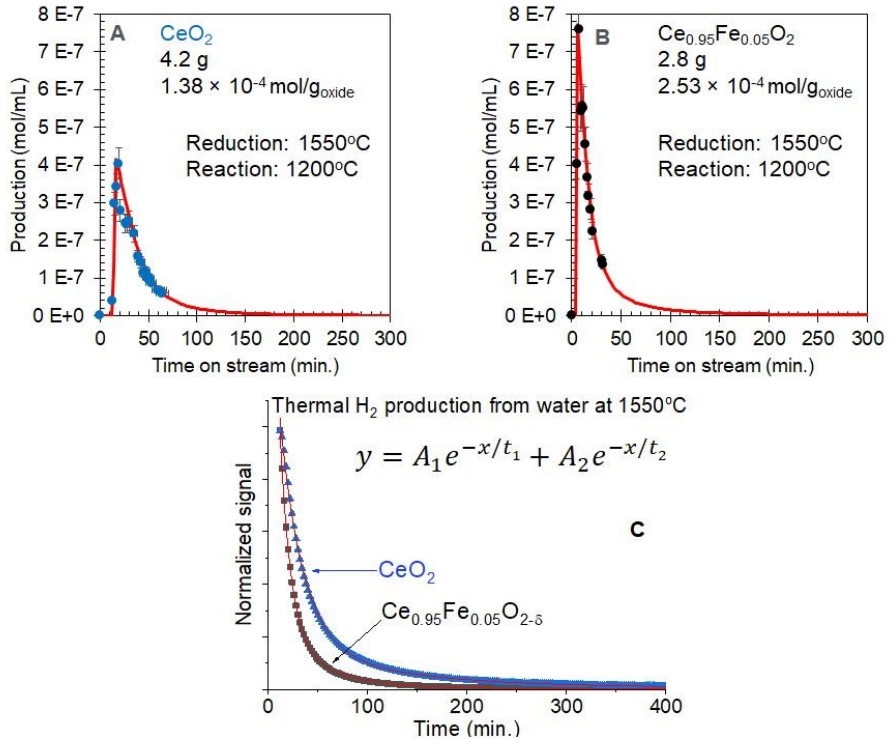

Figure 20.

Thermo-chemical water splitting over CeO_2 (A) and $Ce_{0.95}Fe_{0.05}O_{2-\delta}$ (B) at 1200 °C (1473 K), the oxides were reduced under N_2 at 1550 °C (1823 K) for two hours prior to use. The total amount of H_2 from water per g of oxide is indicated. (C) Normalized fitting of the decay part of H_2 production using a bi-exponential function for both oxides. From Ref. [50], permission License number 6133081449846

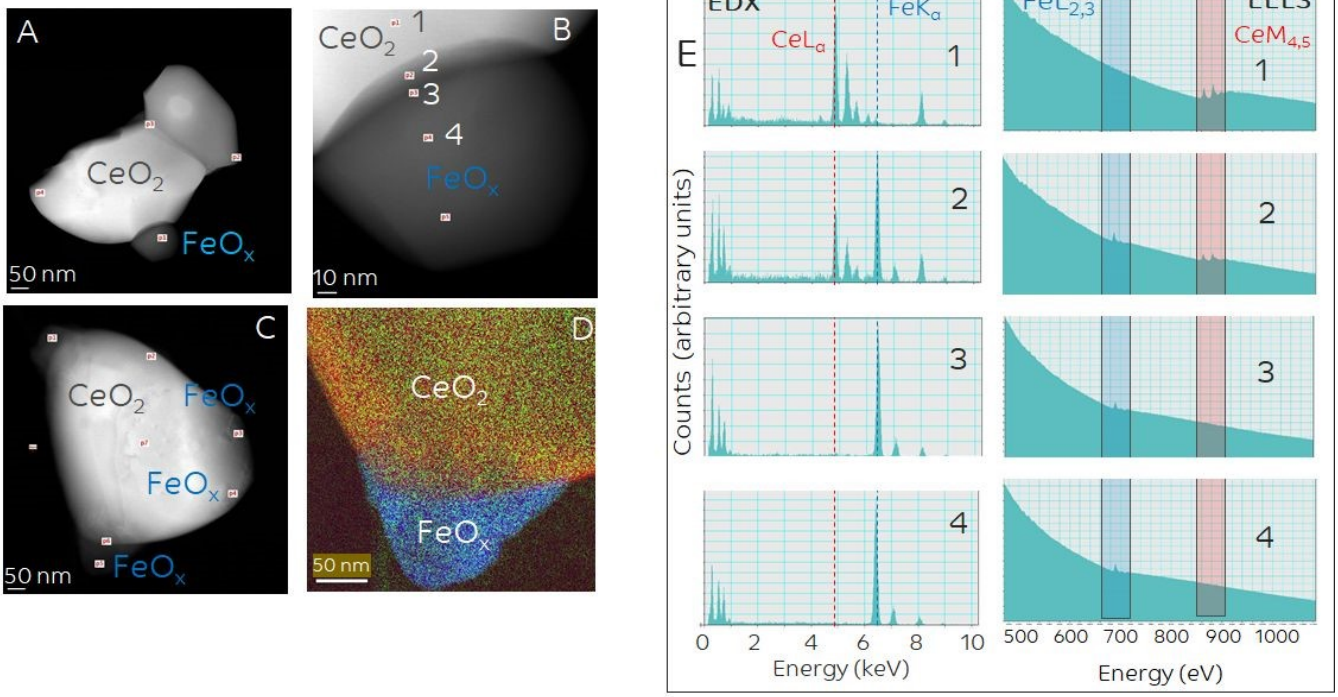

View Article Online
DOI: 10.1039/D6SE00124F

Figure 21.

STEM), EDX, EELS of $Ce_{0.95}Fe_{0.05}O_{2-\delta}$ after the reaction presented in **figure 20**. **A** and **B** are for one particle and **C** and **D** are for another particle. **D**. an elemental EELS map of the particle in **C**. The numbers 1 to 4 in **E** are labeled in B. While segregation of iron to the edges of CeO_2 is seen some iron is still present within the crystallite (also note the presence of FeO_x on the large CeO_2 crystallite in **C**). The crystallite size (TEM) is close to 1μm (an increase of about 200 times when compared to that calcined at 500 °C). Yellow for cerium, blue of iron and red for oxygen atoms. From Ref. [50], permission License number 6133081449846

The activation energy for oxygen diffusion in CeO_2 is typically a small fraction from that needed to reduce it (10-20% or so) [86]. In the process of oxidation of the reduced CeO_2 with water vapor two chemical steps occur. (i) water dissociative adsorption and (ii) oxygen anions diffusion from the surface to the bulk (or V_O diffusion from the bulk to the surface). (i) The first one is different on a stoichiometric surface when compared to defected ones and therefore their kinetic effect on the reaction is expected to be different (water dissociative adsorption over reduced CeO_2 has a stronger energy than that on stoichiometric surface [87]). (ii) The particles have considerably sintered (**Figure 21**) due to heat, so intra particle pore diffusion of water molecules may be neglected. While the increase of the volume to surface ratio upon sintering makes the process mostly bulk driven (since the majority of the oxygen defects would be located in the bulk) the reaction would still be surface driven first if the adsorption of water is a limiting step. While a fraction of Fe oxides has segregated out there is still some Fe inside as seen by EDX and EELS (**figure 21**). It is therefore possible that, in some locations, the interface has the needed gradient concentration of Fe cations to affect the reaction rate when compared to pure CeO_2.

Table 7:

Fitting parameters for the decay part of the H_2 production profile (at 1473 K) from water as a function of time of the pre-reduced oxides at 1823 K. The time constant τ = 1/t. A double exponential decay equation was used $y = A_1 e^{-x/t1} + A_2 e^{-x/t2}$

oxide	A_1 (mol/mL)	t_1 (min)	τ $(min)^{-1}$	A_2 (mol/mL)	t_2 (min)	τ $(min)^{-1}$	t_1/t_2
CeO_2	7.3×10^{-7}	22.5 ± 0.2	0.044	9.7×10^{-8}	108.8 ± 2.9	0.009	0.21
$Ce_{0.95}Fe_{0.05}O_2$	1.2×10^{-6}	10.7 ± 0.06	0.093	1.3×10^{-7}	47.3 ± 0.6	0.021	0.23

From Ref. [50], permission License number 6133081449846

The three following equations summarize the main reactions that occur during water oxidation. Large crystallites of CeO_2 are (111) O-terminated in the fluorite structure and these terminated oxygen anions are bonded to three Ce cations in the second layer, yet for the sake of simplicity it is easier to write them as (Ce-O-Ce) bearing in mind that they are not in the same plane.

View Article Online
DOI: 10.1039/D6SE00124F

10.a. Reaction steps

Electron transfer reaction: water dissociative adsorption on surface oxygen defect followed by oxidation and hydrogen generation.

$$H_2O + [\mathbf{Ce^{3+}}\text{-}V^{s}_{O}\text{-}\mathbf{Ce^{3+}}]_{surface} \rightarrow H_2 + \mathbf{Ce^{4+}}\text{-}O^{2-}\text{-}\mathbf{Ce^{4+}} \qquad \textit{Equation 4}$$

V^{s}_{O} is for a surface oxygen defect and Ce^{3+} is for a reduced cation in the second layer of the (111) terminated surface.

Acid-base interaction: water dissociative adsorption over stoichiometric sites (no charge transfer)

$$H_2O + [\mathbf{Ce^{4+}}\text{-}\mathbf{O^{2-}}\text{-}\mathbf{Ce^{4+}}]_{surface} \rightarrow \mathbf{Ce^{4+}}(^{-}OH)\text{-}\mathbf{O^{2-}}(H^{+})\text{-}\mathbf{Ce^{4+}} \qquad \textit{Equation 5}$$

Diffusion: surface oxygen diffusion into the bulk (or V_O diffusion to the surface) driven by heat and water dissociative adsorption (equations 4 and 5).

$$[\mathbf{Ce^{4+}}\text{-}\mathbf{O^{2-}}\text{-}\mathbf{Ce^{4+}}]_{surface} + [\mathbf{Ce^{3+}}\text{-}V^{b}_{O}\text{-}\mathbf{Ce^{3+}}]_{bulk} \rightarrow [\mathbf{Ce^{3+}}\text{-}V^{s}_{O}\text{-}\mathbf{Ce^{3+}}]_{surface} + [\mathbf{Ce^{4+}}\text{-}\mathbf{O^{2-}}\text{-}\mathbf{Ce^{4+}}]_{bulk}$$

Equation 6

V^{b}_{O} is bulk oxygen defect.

The two protons in equation 5 (of the two surface hydroxyls) become one molecule of hydrogen upon the reaction with two electrons from equation 6.

The substitution of a fraction of Ce cations by Fe cations on the surface and in the bulk affect equations 4 and 6. Equation 5 is an acid-base exchange reaction that is largely not affected by the change in the nature of a metal cation. Although it can be affected by the degree of coordination [88] (such as in different surface structures) this may be neglected here because of the small energy difference. The concentration of V_O has increased in the presence of Fe cations and this affects primarily equation 4. However, the faster kinetics indicate that the dissociative adsorption of water on oxygen vacancy sites is also accelerated when Fe cations are present. Therefore, in the presence of Fe cations in the CeO_2 lattice, equation 6' bellow, is expected to be faster than equation 4 if the dissociative adsorption energy is higher on Fe- V^{s}_{O}-Ce when compared to Ce- V^{s}_{O}-Ce centers.

$$H_2O + [\mathbf{Ce^{3+}}\text{-}V^{s}_{O}\text{-}\mathbf{Fe^{2+}}]_{surface} \rightarrow H_2 + \mathbf{Ce^{4+}}\text{-}O^{2-}\text{-}\mathbf{Fe^{3+}} \qquad \textit{Equation 7'}$$

View Article Online
DOI: 10.1039/D6SE00124F

11. Conclusions

The chemical states of Ce^{3+} cations in $Ce_{1-y}Fe_yO_2$ are analyzed by their deep (XPS Ce3d) and shallow (XPS Ce5p) core levels in addition to their valence level (XPS Ce4f) spectroscopy at different Fe^{3+} concentrations. Moreover, the states of U^{x+} in $Ce_{1-y}U_yO_2$ were further analyzed by their core levels and DFT+U methods. HR-STEM and EELS for the as prepared mixed oxides showed, in line with XRD results, that the cations (Fe^{3+} or U^{4+}) are homogeneously distributed inside CeO_2. While the addition of Fe^{3+} cations doubled the reaction yield and considerably increased the cycle kinetics, phase segregation occurred upon thermochemical water splitting reaction when the mixed oxide was reduced by heating in an inert environment at 1550 ^oC. A three-step mechanism for the water splitting reaction is presented in which the dissociative adsorption, the bulk diffusion of oxygen anions and the hydrogen re-combinative desorption are discussed. Results point to the role of Ce-O-Fe sites in improving the reaction kinetics, yet the considerable sintering indicates that maintaining oxide homogeneity is needed for long-term stability. In the case of $Ce_{1-y}U_yO_2$, the TCWSR to H_2 is sensitive to the content of U, where low percentages of U cations considerably enhanced the production. This enhancement is attributed to the increase in Ce^{4+} cations reduction to Ce^{3+} cations. The trend of this Ce^{4+}/Ce^{3+} conversion studied by *in situ* XPS of single crystalline mixed oxides showed evidence of charge transfer ($Ce^{4+} + U^{4+} \rightarrow Ce^{3+} + U^{5+}$) at low U content. Evidence of charge transfer was further obtained computationally using the DFT + U method, giving more support to the experimental Ce^{4+}/Ce^{3+} and $U^{4+}/U^{5+}/U^{6+}$ results. This charge-transfer effect is sensitive to the local distribution of U^{4+} cations in the ceria lattice. One of the key conclusions is the need to lower the reduction temperature of the mixed oxide phase considerably to prevent phase separation. There is also a need to further study the entropical effect of the mixed oxides on the reduction of the host material, as it appears to be an important factor for the charge transfer reaction. Several strategies are discussed to mitigate phase segregation in ceria-based redox materials, including maintaining low dopant concentrations to preserve solid solutions, selecting dopants with compatible ionic radii and crystal structures, and employing synthesis methods that promote homogeneous cation distribution.

Conflicts of interest

The author declares no conflicts of interest.

Data availability Statement

All data are available upon request from the author.

References

View Article Online
DOI: 10.1039/D6SE00124F

[1] Christopher L. Muhich, Brian D. Ehrhart, Ibraheam Al-Shankiti, Barbara J. Ward, Charles B. Musgrave and Alan W. Weimer, *WIREs Energy Environ.*, 2016, **5**, 261–287, DOI: 10.1002/wene.174.

[2] Danielle Schweke, Yuval Mordehovitz, Mahdi Halabi, Lee Shelly and Shmuel Hayun, *Adv. Mater.*, 2018, **30**, 1706300, DOI: 10.1002/adma.201706300.

[3] Ibraheam Al-Shankiti, Yong Man Choi, Faisal M. Al-Otaibi and Hicham Idriss, *Catalyst for thermochemical water splitting*, US Pat., US9421537, 2016; US Pat., US9675961, 2017.

[4] Srirat Chuayboon and Stéphane Abanades, *Int. J. Hydrogen Energy*, 2020, **45**, 25783–25810, DOI: 10.1016/j.ijhydene.2020.04.098.

[5] Yanpeng Mao, Yibo Gao, Wei Dong, Hongyi Wu, Zhe Song, Xiao Zhao, Jian Sun and Wenlong Wang, *Appl. Energy*, 2020, **267**, 114860, DOI: 10.1016/j.apenergy.2020.114860.

[6] F. M. Pinto, V. Y. Suzuki, R. C. Silva and F. A. La Porta, *Front. Mater.*, 2019, **6**, 260, DOI: 10.3389/fmats.2019.00260.

[7] Tingting Lin, Xin Lv, Zhineng Hu, Aoshu Xu and Caihui Feng, *Sensors*, 2019, **19**, 233, DOI: 10.3390/s19020233.

[8] Tiziano Montini, Michele Melchionna, Matteo Monai and Paolo Fornasiero, *Chem. Rev.*, 2016, **116**, 5987–6041, DOI: 10.1021/acs.chemrev.5b00603.

[9] Ubong Johnson Etim, Yibing Song and Ziyi Zhong, *Front. Energy Res.*, 2020, **8**, 545431, DOI: 10.3389/fenrg.2020.545431.

[10] Katsumi Taniya, Yoshihiko Horie, Ryo Fujita, Yuki Ichihashi and Shusaku Nishiyama, *Appl. Catal. B Environ.*, 2023, **330**, 122568, DOI: 10.1016/j.apcatb.2023.122568.

[11] David A. Andersson, Sergei I. Simak, Nina V. Skorodumova, Igor A. Abrikosov and Börje Johansson, *Appl. Phys. Lett.*, 2007, **90**, 031909, DOI: 10.1063/1.2431775.

[12] Benjamin E. Hanken, Christopher R. Stanek, Niels Grønbech-Jensen and Mark Asta, *Phys. Rev. B*, 2011, **84**, 085131, DOI: 10.1103/PhysRevB.84.085131.

[13] Jessica Scaranto and Hicham Idriss, *Top. Catal.*, 2015, **58**, 143–148, DOI: 10.1007/s11244-014-0353-x.

[14] Masato Kato, Masashi Watanabe, Shun Hirooka and Romain Vauchy, *Front. Nucl. Eng.*, 2023, **1**, 1081473, DOI: 10.3389/fnuen.2022.1081473.

[15] Massimo Moser, Matteo Pecchi and Thomas Fend, *Energies*, 2019, **12**, 352, DOI: 10.3390/en12030352.

[16] Hicham Idriss, *Inorganics*, 2024, **12**, 42, DOI: 10.3390/inorganics12020042.

[17] Yukio Hinatsu and Takeo Fujino, *J. Solid State Chem.*, 1988, **76**, 124–130, DOI: 10.1016/0022-4596(88)90199-5.42. https://doi.org/10.3390/inorganics12020042.

[18] Lee Shelly, Danielle Schweke, Shimon Zalkind, Noah Shamir, Shmuel Barzilai, Thomas Gouder and Shmuel Hayun, *Chem. Mater.*, 2018, **30**, 8650–8660, DOI: 10.1021/acs.chemmater.8b03894.

[19] Damien Prieur, Jean-François Vigier, Karin Popa, Olaf Walter, Oliver Dieste, Zsolt Varga, Aaron Beck, Tonya Vitova, Andreas C. Scheinost and Philippe M. Martin, *Inorg. Chem.*, 2021, **60**, 14550–14556, DOI: 10.1021/acs.inorgchem.1c01071. https://doi.org/10.1021/acs.inorgchem.1c01071.

[20] Yahya Al-Salik, Ibraheam Al-Shankiti and Hicham Idriss, *J. Electron Spectrosc. Relat. Phenom.*, 2014, **194**, 66–73, DOI: 10.1016/j.elspec.2013.11.013.

[21] Hicham Idriss, Ibraheam Al-Shankiti, Yong-Man Choi and Faisal M. Al-Otaibi, *Catalyst for thermochemical water splitting*, US Pat., US9675961, 2017.

View Article Online
DOI: 10.1039/D6SE00124F

[22] Carlos Morales, Rudi Tschammer, Thomas Gouder, YongMan Choi, Dalaver Anjum, Aman Baunthiyal, Jon-Olaf Krisponeit, Jens Falta, Jan Ingo Flege and Hicham Idriss, *J. Phys. Energy*, 2025, **7**, 025012, DOI: 10.1088/2515-7655/adbad9.

[23] Lei Cheng, Xiaoyang Yue, Jiajie Fan and Quanjun Xiang, *Adv. Mater.*, 2022, **34**, e2200929, DOI: 10.1002/adma.202200929.

[24] Shuo Zhao, Dandan Kang, Yiheng Liu, Yongfeng Wen, Xiaopeng Xie, Haimin Yi and Xuefeng Tang, *ACS Catal.*, 2020, **10**, 11739–11750, DOI: 10.1021/acscatal.0c02832.

[25] Kiyong Ahn, Dong-Su Yoo, Dinesh H. Prasad, Hee-Woong Lee, Yong-Chae Chung and Jong-Heun Lee, *Chem. Mater.*, 2012, **24**, 4261–4267, DOI: 10.1021/cm3022424.

[26] Meng Zhang, Dong Jiang and Hua Jiang, *Mater. Res. Bull.*, 2012, **47**, 4006–4012, DOI: 10.1016/j.materresbull.2012.07.012.

[27] Matthew D. Krcha and Michael J. Janik, *Langmuir*, 2013, **29**, 10120–10131, DOI: 10.1021/la401747n.

[28] Giulia Righi, Silvia Benedetti and Rita Magri, *J. Phys. Condens. Matter*, 2022, **34**, 204010, DOI: 10.1088/1361-648X/ac58d9.

[29] Michael Nolan, *J. Mater. Chem.*, 2011, **21**, 9160–9168, DOI: 10.1039/C1JM11238D.

[30] Xinquan Wang, Manqi Shen, Jian Wang and Stefano Fabris, *J. Phys. Chem. C*, 2010, **114**, 10221–10228, DOI: 10.1021/jp101100f.

[31] Steffen Grieshammer, Benjamin O. H. Grope, Julius Koettgen and Manfred Martin, *Phys. Chem. Chem. Phys.*, 2014, **16**, 9974–9986, DOI: 10.1039/C3CP54811B.

[32] Xiong-Shan Liu, Xu-Dong Wang, Min Yao, Wei Cui and Hui Yan, *Catal. Commun.*, 2015, **63**, 35–40, DOI: 10.1016/j.catcom.2014.09.032.

[33] Hsin-Tsung Chen and Jee-Gong Chang, *Phys. Chem. C* 2011, **115**, **30**, 14745–14753, DOI: 10.1021/jp201231d.

[34] Yang Yu, Mingjia Zhang, Huangang Shi, Jifa Qu, Yongheng Xiong, Wenyi Tan, Xinlei Ge, and Qijie Jin, *J. Environ. Sci.,* 2025, **158**, 39-49, DOI: 10.1016/j.jes.2025.02.001.

[35] Steffen Grieshammer, Sebastian Eisele, and Julius Koettgen, *J. Phys. Chem. C* **2018**, 122, 18809−18817, DOI: 10.1021/acs.jpcc.8b04361

[36] Zheng Hu and Horia Metiu, *J. Phys. Chem. C*, 2011, **115**, 17898–17909, DOI: 10.1021/jp203774u.

[37] Muhammad Alaydrus, Masayuki Sakaue and Hirofumi Kasai, *Phys. Chem. Chem. Phys.*, 2016, **18**, 12938–12946, DOI: 10.1039/C6CP00637J.

[38] Stephan P. Waldow and Roger A. De Souza, *J. Phys. Energy*, 2020, **2**, 024001, DOI: 10.1088/2515-7655/ab5cfd.

[39] Hui Wang, Zhen Qu, Haoran Xie, Nobuyuki Maeda, Liang Miao and Zhan Wang, *J. Catal.*, 2016, **338**, 56–67, DOI: 10.1016/j.jcat.2016.02.009.

[40] Maria Lykaki, Sofia Stefa, Sónia A. C. Carabineiro, Pavlos K. Pandis, Vassilis N. Stathopoulos and Michalis Konsolakis, *Catalysts*, 2019, **9**, 371, DOI: 10.3390/catal9040371.

[41] Sayeda Halima Beguma, Chin-Te Hung, Yit-Tsong Chen, Shing-Jong Huang, Pei-Hao Wu, Xiaoxiang Han and Shang-Bin Liu, *J. Mol. Catal. A: Chem.*, 2016, **423**, 423–432, DOI: 10.1016/j.molcata.2016.07.036

View Article Online
DOI: 10.1039/D6SE00124F

[42] Hui Wang, Zhenping Qu, Hongbin Xie, Nobutaka Maeda, Lei Miao, Zhong Wang, *J. Catal.* 2016, **338** ,56–67, https://doi.org/10.1016/j.jcat.2016.02.009

[43] Maria Lykaki, Sofia Stefa, Sónia A. C. Carabineiro,Pavlos K. Pandis, Vassilis N. Stathopoulos, and Michalis Konsolakis, *Catalysts* 2019*,* **9***,* 371, https://doi.org/10.3390/catal9040371

[44] María Orfila, Daniel Sanz, María Linares, Raúl Molina, Raúl Sanz, Javier Marugán, Juan Ángel Botas, *Int. J. Hydrogen Energy*, 2021, **46**, 17458–17471, DOI: 10.1016/j.ijhydene.2020.04.222.

[45] Adetunji Onigbajumo, Priyanka Swarnkar, Geoffrey Will, Thirumalachari Sundararajan, Alireza Taghipour, Sara Couperthwaite, Ted Steinberg and Thomas Rainey, *J. Clean. Prod.*, 2022, **371**, 133303, DOI: 10.1016/j.jclepro.2022.133303.

[46] William C. Chueh, Christian Falter, Michael Abbott, David Scipio, Philipp Furler, Sossina M. Haile and Aldo Steinfeld, *Science*, 2010, **330**, 1797–1801, DOI: 10.1126/science.1197834.

[47] Sandro Ackermann, John Scheffe and Aldo Steinfeld, *J. Phys. Chem. C*, 2014, **118**, 5216–5225, DOI: 10.1021/jp411717m.

[48] Ricardo Grau-Crespo, Nora H. de Leeuw, Saad Hamad and Umesh V. Waghmare, *Proc. R. Soc. A*, 2011, **467**, 1925–1938, DOI: 10.1098/rspa.2010.0582.

[49] Alex Le Gal, Stéphane Abanades and Gilles Flamant, *Energy Fuels*, 2011, **25**, 4836–4845.

[50] Salim Al-Taweel, Muhammad A. Nadeem, Hicham Idriss, *Energy Technol.,* 2022, **10**, 2100491. https://doi.org/10.1002/ente.202100491.

[51] Ki Hwan Ahn, Dong Seok Yoo, Dinesh H. Prasad, Hyun-Woo Lee, Yong-Cheol Chung and Jae-Hyeong Lee, *Chem. Mater.*, 2012, **24**, 4261–4267, DOI: 10.1021/cm3023399.

[52] Darwin Arifin, Andrea Ambrosini, Steven A. Wilson, Bennett Mandal, Christopher L. Muhich and Alan W. Weimer, *Int. J. Hydrogen Energy*, 2020, **45**, 160–174, DOI: 10.1016/j.ijhydene.2019.10.177.

[53] Hideo Kaneko, Tetsuya Miura, Hiroshi Ishihara, Satoshi Taku, Takahisa Yokoyama, Hidenori Nakajima and Yasuyuki Tamaura, *Energy*, 2007, **32**, 656–663, DOI: 10.1016/j.energy.2006.06.018.

[54] Meng Zhang, Dongsheng Jiang, Haifeng Jiang, *Mater. Res. Bull.,* 2012*,* **47** ,4006–4012, https://doi.org/10.1016/j.materresbull.2012.07.012.

[55] T. Dhanni, S. Jayalekshmi, M. C. S. Kumar, T. P. Rao and A. C. Bose, *J. Phys. Chem. Solids*, 2010, **71**, 1020–1025, DOI: 10.1016/j.jpcs.2010.04.011

[56] G. D. Takalkar, R. R. Bhosale, A. Kumar, F. AlMomani, M. Khraisheh, R. A. Shakoor, R. B. Gupta, *Sol. Energy*, 2018, **172**, 204–211, DOI: 10.1016/j.solener.2018.03.022

[57] M. Strehle, *X-Ray Photoelectron Spectroscopy (XPS) Study of Single Crystal UO_2 and U_3O_8 on R-Plane and Y Stabilized Zirconium (YSZ) Substrates*, MSc thesis, University of Illinois at Urbana-Champaign, 2011.

[58] Henry R. Hoekstra, Stanley Siegel and Francis X. Gallagher, *J. Inorg. Nucl. Chem.*, 1970, **32**, 3237–3248, DOI: 10.1016/0022-1902(70)80206-8

[59] Gregorie C. Allen and N. R. Holmes, *J. Nucl. Mater.*, 1995, **223**, 231–237, DOI: 10.1016/0022-3115(95)00025-9

[60] Anders Magnéli, Lars Kihlborg, H. Holtermann, J. S. Sörensen and N. A. Sörensen, *Acta Chem. Scand.*, 1951, **5**, 578–580, DOI: 10.3891/acta.chem.scand.05-0578.

View Article Online
DOI: 10.1039/D6SE00124F

[61] Hiroaki Tagawa, Takeo Fujino, Kenju Watanabe, Yumiko Nakagawa and Koji Saita, *Bull. Chem. Soc. Jpn.*, 1981, **54**, 138–142, DOI: 10.1246/bcsj.54.138.

[62] K. Suresh Kumar, T. Mathews, H. P. Nawada and N. P. Bhat, *J. Nucl. Mater.*, 2004, **324**, 177–182, DOI: 10.1016/j.jnucmat.2003.09.014.

[63] Ibraheam Al-Shankiti, Faisal Al-Otaibi, Yahya Al-Salik and Hicham Idriss, *Top. Catal.*, 2013, **56**, 1129–1138, DOI: 10.1007/s11244-013-0079-1

[64] Sayeda Halima Beguma, Chin-Te Hunga, Yit-Tsong Chena, Shing-Jong Huangc, Pei-Hao Wu, Xiaoxiang Hand, Shang-Bin Liu, *Journal of Molecular Catalysis A: Chemical* 2016, **423**, 423–432, http://dx.doi.org/10.1016/j.molcata.2016.07.036.

[65] Konstantin I. Maslakov, Yury A. Teterin, Aleksej J. Popel, Anton Yu. Teterin, Kirill E. Ivanov, Stepan N. Kalmykov, Vladimir G. Petrov, Peter K. Petrov and Ian Farnan, *Appl. Surf. Sci.*, 2018, **448**, 154–162.

[66] Konstantin I. Maslakov, Yury A. Teterin, Mikhail V. Ryzhkov, Aleksej J. Popel, Anton Yu. Teterin, Kirill E. Ivanov, Stepan N. Kalmykov, Vladimir G. Petrov, Peter K. Petrov and Ian Farnan, *Phys. Chem. Chem. Phys.*, 2018, **20**, 16167–16175, DOI: 10.1039/C8CP01442F

[67] S. Eck, C. Castellarin-Cudia, S. Surnev, M. G. Ramsey and F. P. Netzer, *Surf. Sci.*, 2002, **520**, 173–185, DOI: 10.1016/S0039-6028(02)02272-0.

[68] Yury A. Teterin, Serguei V. Stefanovskij, Serguei V. Yudintsev, George N. Bek-Uzarov, Anton Yu. Teterin, Konstantin I. Maslakov and Igor O. Utkin, *Nucl. Technol. Radiat. Prot.*, 2004, **19**, 31–38, DOI: 10.2298/NTRP0401031T

[69] Gareth S. Parkinson, *Surf. Sci. Rep.*, 2016, **71**, 272–365, DOI: 10.1016/j.surfrep.2016.02.001

[70] A. N. Mansour and R. A. Brizzolara, *Surf. Sci. Spectra*, 1996, **4**, 345–350, DOI: 10.1116/1.1247831

[71] M. Preisinger, M. Krispin, T. Rudolf, S. Horn and D. R. Strongin, *Phys. Rev. B*, 2005, **71**, 165409, DOI: 10.1103/PhysRevB.71.165409

[72] T. Radu, C. Iacovita, D. Benea and R. Turcu, *Appl. Surf. Sci.*, 2017, **405**, 337–343, DOI: 10.1016/j.apsusc.2017.02.002

[73] A. P. Grosvenor, B. A. Kobe and N. S. McIntyre, *Surf. Sci.*, 2004, **572**, 217–227, DOI: 10.1016/j.susc.2004.08.035

[74] W. Temesghen and P. Sherwood, *Anal. Bioanal. Chem.*, 2002, **373**, 601–608, DOI: 10.1007/s00216-002-1362-3

[75] Paul S. Bagus, Connie J. Nelin, C. R. Brundle, B. Vincent Crist, N. Lahiri and Kevin M. Ross, *J. Chem. Phys.*, 2021, **154**, 094709, DOI: 10.1063/5.0039765

[76] M. Fondell, M. Gorgoi, M. Boman and A. Lindblad, *J. Electron Spectrosc. Relat. Phenom.*, 2018, **224**, 23–26, DOI: 10.1016/j.elspec.2017.09.008.

[77] Takashi Hasegawa, S. M. F. Shahed, Yuta Sainoo, Ayumi Beniya, Naoki Isomura, Yusuke Watanabe and Takashi Komeda, *J. Chem. Phys.*, 2014, **140**, 044711, DOI: 10.1063/1.4849595.

[78] Matthias Sauerbrey, Jan Höcker, Marco Wellbrock, Markus Schowalter, Jan-Olaf Krisponeit, Kai Müller-Caspary, Andreas Rosenauer, Gaofeng Wei, Luca Colombi Ciacchi, Jürgen Falta and Jan Ingo Flege, *Cryst. Growth Des.*, 2016, **16**, 4216–4224, DOI: 10.1021/acs.cgd.6b00192.

View Article Online
DOI: 10.1039/D6SE00124F

[79] Jan Ingo Flege, Jan Höcker, Bastian Kaemena, T. O. Menteş, Alessandro Sala, Armin Locatelli, Saptarshi Gangopadhyay, J. T. Sadowski, S. D. Senanayake, Jürgen Falta, *Nanoscale*, 2016, **8**, 10849–10856, DOI: 10.1039/C6NR02393B.

[80] David C. Grinter and Geoffrey Thornton, *J. Phys. Condens. Matter*, 2022, **34**, 253001, DOI: 10.1088/1361-648X/ac5d89.

[81] Yuan Zhang, Wenfeng Feng, Fan Yang and Xinhe Bao, *Chin. J. Catal.*, 2019, **40**, 204–213, DOI: 10.1016/S1872-2067(18)63171-7.

[82] Ghada El Jamal, Thomas Gouder, Rachel Eloirdi, Hicham Idriss and Mats Jonsson, *J. Phys. Chem. C*, 2023, **127**, 14222–14231, DOI: 10.1021/acs.jpcc.3c02795

[83] Ine Arts, Rolando Saniz, Gianguido Baldinozzi, Gregory Leinders, Marc Verwerft, Dirk Lamoen, *J. Nucl. Mater.*, 2024, **599**, 155249, DOI: 10.1016/j.jnucmat.2024.155249.

[84] Feng Tao, Michael E. Grass, Yawen Zhang, Derek R. Butcher, James R. Renzas, Zhi Liu, Jen Y. Chung, Bongjin S. Mun, Miquel Salmeron and Gabor A. Somorjai, *Science*, 2009, **322**, 932–934, DOI: 10.1126/science.1164170.

[85] A. Lidor, Y. Aschwanden, J. Häseli, P. Reckinger, P. Haueter, A. Steinfeld, *Applied Energy,* 2023, **329**, 120211 (1-11). https://doi.org/10.1016/j.apenergy.2022.120211

[86] Darwin Arifin, Andrea Ambrosini, Steven A. Wilson, Bennett Mandal, Christopher L. Muhich, Alan W. Weimer, *Int. J. Hydrogen Energy*, 2020, **45**, 160-174, https://doi.org/10.1016/j.ijhydene.2019.10.177

[87] David R. Mullins, Peter M. Albrecht, Tsung-Liang Chen, Florencia C. Calaza, Michael D. Biegalski, Hans M. Christen and Steven H. Overbury, *J. Phys. Chem. C*, 2012, **116**, 19419–19428, DOI: 10.1021/jp306444h.

[88] S. Fuente, Maria M. Branda and Francesc Illas, *Theor. Chem. Acc.*, 2012, **131**, 1190, DOI: 10.1007/s00214-012-1190-2

View Article Online
DOI: 10.1039/D6SE00124F

Data Availability Statement

No primary research results, software or code have been included and no new data were generated or analysed as part of this review.